



Defence Research and
Development Canada

Recherche et développement
pour la défense Canada



Optimization of CRIPT detector performance

Richard Hydomako

The scientific or technical validity of this Contract Report is entirely the responsibility of the contractor and the contents do not necessarily have the approval or endorsement of Defence R&D Canada.

Defence R&D Canada – Ottawa

Contract Report
DRDC Ottawa CR 2013-127
January 2014

Canada

Optimization of CRIPT detector performance

Richard Hydomako

Prepared by:

Calian Technologies Ltd.

340 Legget Drive, Suite 101, Ottawa, ON Canada K2K 1Y6

Project Manager: David Waller

Contract Number: EN578-120158/234/EI

Contract Scientific Authority: David Waller

The scientific or technical validity of this Contract Report is entirely the responsibility of the contractor and the contents do not necessarily have the approval or endorsement of Defence R&D Canada.

Defence R&D Canada – Ottawa

Contract Report

DRDC Ottawa CR 2013-127

January 2014

Scientific Authority

Original signed by David Waller

David Waller

Approved by

Original signed by B. Katsube

B. Katsube

Head, Radiological and Nuclear Defence and Navigation Electronic Warfare

Approved for release by

Original signed by C. McMillan

C. McMillan

Chief Scientist, DRDC, Ottawa Research Centre

- © Her Majesty the Queen in Right of Canada as represented by the Minister of National Defence, 2014
- © Sa Majesté la Reine (en droit du Canada), telle que représentée par le ministre de la Défense nationale, 2014

Abstract

The Cosmic Ray Inspection and Passive Tomography (CRIPT) collaboration has constructed a large-scale detector prototype for investigating the use of cosmic ray muon scattering tomography for Special Nuclear Material (SNM) identification. In order to produce reconstructed images of the highest quality, it is important to ensure that the detector has achieved optimal performance. In this report, the detector operating parameters are investigated, with the goal of optimizing the hit resolution. Furthermore, the results of simple Monte Carlo simulation are presented, which validate the observed geometric acceptance of the detector and give a rough evaluation of the performance of the momentum estimate algorithm.

Résumé

La collaboration « Inspection et tomographie passive par rayonnement cosmique » (CRIPT, de l'anglais Cosmic Ray Inspection and Passive Tomography) a construit le prototype d'un grand détecteur pour étudier l'utilisation de la tomographie par diffusion de muons produits par les rayons cosmiques afin de détecter les matières nucléaires spéciales (MNS). Afin de produire des images reconstruites de très haute qualité, il est important de s'assurer que le détecteur offre une performance optimale. Le présent rapport fait état des travaux visant à étudier les paramètres opérationnels du détecteur, et à optimiser la résolution des impacts. De plus, les résultats d'une simulation Monte-Carlo simple sont présentés : ils valident l'acceptation géométrique observée du détecteur et ils donnent une évaluation approximative de la performance de l'algorithme de destination de la quantité de mouvement.

This page intentionally left blank.

Executive summary

Optimization of CRIPT detector performance

Richard Hydromako; DRDC Ottawa CR 2013-127; Defence R&D Canada – Ottawa; January 2014.

Background: The Cosmic Ray Inspection and Passive Tomography (CRIPT) project has constructed a large-scale prototype detector for the identification of Special Nuclear Material (SNM). This detector measures the scattering of through-going cosmic ray muons to infer the three-dimensional density of objects in the detector imaging volume. The detector performance is an important factor in the production of good-quality reconstructed images. In this report, the optimization of optimization parameters for the CRIPT detector is presented. Additionally, a simple Monte Carlo simulation study was performed with the goal of validating the overall detector performance.

Principal results: By systematically varying the set-voltage for the photomultiplier tubes (PMTs) and data acquisition system (DAQ) threshold values, an optimal set of operating parameters was arrived at that minimized the detector hit resolution. Moreover, a bandwidth issue in the DAQ system was identified and a mitigating solution implemented such that the number of usable muon tracks was increased by 17%. Finally, the Monte Carlo simulation validated the observed detector acceptance and performance of the momentum estimate algorithm.

Significance of results: The results of this study help to improve the operation of the CRIPT detector as well as provide a performance evaluation focusing on the Upper and Lower Tracker sections. The recommended operating parameters should optimize the hit resolution and thereby improve the overall imaging reconstruction. Likewise, the validation of the geometric acceptance using a simple Monte Carlo simulation should provide confidence that the CRIPT detector is functioning correctly.

Sommaire

Optimization of CRIPT detector performance

Richard Hydomako ; DRDC Ottawa CR 2013-127 ; R & D pour la défense Canada
– Ottawa ; janvier 2014.

Contexte : Dans le cadre du projet « Inspection et tomographie passive par rayonnement cosmique » (CRIPT, de l'anglais Cosmic Ray Inspection and Passive Tomography), le prototype d'un grand détecteur a été construit pour étudier l'utilisation de la tomographie par diffusion de muons produits par les rayons cosmiques pour détecter les matières nucléaires spéciales (MNS). Ce détecteur mesure la diffusion des muons produits par les rayons cosmiques et traversant les objets afin de déduire la densité tridimensionnelle de ces objets dans le volume imagé par le détecteur. La performance du détecteur est un facteur important pour produire des images reconstruites de bonne qualité. Dans le présent rapport, les auteurs présentent les paramètres d'optimisation du détecteur CRIPT. En outre, une simulation Monte-Carlo simple a été réalisée afin de valider la performance globale du détecteur.

Résultats principaux : En variant systématiquement la tension de consigne des tubes photomultiplicateurs (PMT) et les valeurs seuils du système d'acquisition de données (DAD), on a obtenu un ensemble optimal de paramètres opérationnels qui minimise la résolution des impacts dans le détecteur. De plus, un problème de largeur de bande dans le système DAD a été constaté, et une solution a été trouvée qui a permis d'atténuer le problème, de sorte que le nombre de trajectoires de muons utilisables a augmenté de 17%. Enfin, la simulation Monte-Carlo a validé l'acceptation géométrique observée du détecteur et la performance de l'algorithme de destination de la quantité de mouvement.

Portée des résultats : Les résultats de cette étude aident à améliorer le fonctionnement du détecteur CRIPT et ils permettent d'évaluer la performance des sections de suivi supérieure et inférieure. Les paramètres opérationnels recommandés devraient optimiser la résolution des impacts, et ainsi améliorer la reconstruction globale des images. Par ailleurs, la validation de l'acceptation géométrique, au moyen d'une simulation Monte-Carlo simple, devrait permettre d'avoir confiance dans le bon fonctionnement du détecteur CRIPT.

Acknowledgements

The author would like to thank Dr. Khalil Boudjemline, who did much of the hard work putting together the CRIPT analysis suite.

This page intentionally left blank.

Table of contents

Abstract	i
Résumé	i
Executive summary	iii
Sommaire	iv
Acknowledgements	v
Table of contents	vii
List of figures	ix
List of tables	x
1 Introduction	1
1.1 Detector overview	1
2 Data acquisition system performance	2
3 PMT high-voltage scan	4
3.1 Hit resolution	5
3.2 Efficiency	5
3.3 Recommendation	8
4 Threshold scan	8
4.1 Recommendation	8
5 Monte Carlo simulation	10
5.1 Geometric acceptance	11
5.2 Momentum estimate	12
6 Conclusion	13
References	15

Annex A: Resolution and efficiency summary plots	17
Annex B: Resolution and efficiency plots as a function of voltage	21
Annex C: Resolution map plots	39
Annex D: Occupancy plots for data and simulation	43
Annex E: Reconstructed track theta plots for data and simulation	47

List of figures

Figure 1:	Simplified diagram of the CRIPT detector, showing only the position of the scintillator layers and steel plates (not to scale).	2
Figure 2:	Simplified diagram of the DAQ architecture	3
Figure 3:	Resolution measurement for Plane 8: a) the hit resolution as a function of position along the plane, b) histogram of the measured resolution values, c) summary of measured hit resolutions as a function of PMT set-voltage.	6
Figure 4:	Efficiency measurement for Plane 8: a) the efficiency as a function of position along the plane, b) histogram of the measured efficiency values, c) summary of measured efficiency as a function of PMT set-voltage.	7
Figure 5:	Pulse-height distribution for bar 21, plane 4 at PMT voltage 900V.	9
Figure 6:	Plane resolutions as a function of ADC threshold for the Upper and Lower Trackers.	9
Figure 7:	Resolution map for Plane 8	10
Figure 8:	Comparison of bar occupancy distributions between data (a) and simulation (b) for plane 8.	11
Figure 9:	Comparison of θ_x distributions for reconstructed track angles between data (a) and simulation (b) for plane 8.	12
Figure 10:	Comparison between the simulated and reconstructed muon momentum (note the log colour scale).	13
Figure 11:	Reconstructed muon momentum estimate performance.	14
Figure A.1:	Summary plots of resolutions and efficiencies as a function of set-voltage for the Lower Tracker.	18
Figure A.2:	Summary plots of resolutions and efficiencies as a function of set-voltage for the Upper Tracker.	19
Figure B.1:	Resolution measurements for Plane 4	22
Figure B.2:	Efficiency measurements for Plane 4	23

Figure B.3: Resolution measurements for Plane 5	24
Figure B.4: Efficiency measurements for Plane 5	25
Figure B.5: Resolution measurements for Plane 6	26
Figure B.6: Efficiency measurements for Plane 6	27
Figure B.7: Resolution measurements for Plane 7	28
Figure B.8: Efficiency measurements for Plane 7	29
Figure B.9: Resolution measurements for Plane 8	30
Figure B.10: Efficiency measurements for Plane 8	31
Figure B.11: Resolution measurements for Plane 9	32
Figure B.12: Efficiency measurements for Plane 9	33
Figure B.13: Resolution measurements for Plane 10	34
Figure B.14: Efficiency measurements for Plane 10	35
Figure B.15: Resolution measurements for Plane 11	36
Figure B.16: Efficiency measurements for Plane 11	37
Figure C.1: Lower tracker resolution maps	40
Figure C.2: Upper tracker resolution maps	41
Figure D.1: Occupancy plots for the Lower Tracker (data and simulation).	44
Figure D.2: Occupancy plots for the Lower Tracker (data and simulation).	45
Figure E.1: Lower Tracker reconstructed track $\theta_{(x,y)}$ distributions.	48
Figure E.2: Upper Tracker reconstructed track $\theta_{(x,y)}$ distributions.	49

List of tables

Table 1: Data runs for high-voltage scan.	4
Table 2: List of dataruns for the threshold scan (PMT set-voltage 900V).	8

1 Introduction

The Cosmic Ray Inspection and Passive Tomography (CRIPT) project is an effort to construct a novel cosmic ray muon detector for the purposes of identifying Special Nuclear Material (SNM) [1, 2]. The CRIPT collaboration has constructed a large-scale prototype at Carleton University to investigate the merits of muon scattering tomography, wherein the three-dimensional density of a scanned object is inferred by the measured scattering of through-going charged particles. Extremely dense materials, such as SNM, can then be identified within the large three-dimensional scanning volume of the CRIPT detector.

It is important to evaluate the operation of the detector, especially as a means of performance optimization. A sub-optimally configured detector will take longer to scan objects, and the resulting images will be of poorer quality. This report details a series of analyses that quantify the performance of the detector planes, specifically looking to set the operating parameters such as to optimize the key metrics of resolution and efficiency. Additionally, a Monte Carlo simulation is used to investigate the geometric acceptance of the CRIPT detector. Finally, the simulation is used to validate the implementation of the momentum estimate algorithm.

1.1 Detector overview

The CRIPT detector (Fig. 1) is comprised of twelve $2\text{m} \times 2\text{m}$ planes of triangular scintillator bars. Each plane contains 121 individual scintillator bars, which are 2m long and have a triangular cross-section with a base of 3.23 cm and height of 1.65 cm. The scintillator bars are arranged in a close-fitting pattern of alternating right-side-up and up-side-down bars such that there are no gaps across the plane surface. The scintillated light from each individual bar is collected by a wavelength-shifting optical fiber which is coupled to a 64-channel photo-multiplying tube (PMT) readout device (two PMTs are needed to read out each plane).

Furthermore, the CRIPT detector is divided into six layers, where each layer contains two planes arranged orthogonally. Two layers are located above the imaging volume and are referred to as the Upper Tracker (UT), two layers are located directly below the imaging volume and are referred to as the Lower Tracker (LT), and the final two layers are located below the LT and are referred to as the Spectrometer (SPEC). Note that this report is mainly focused on the optimization of the performance of the UT and LT layers, as these layers are responsible for the tracking used for reconstructive imaging. The SPEC layers are largely ignored, as the multiple-scattering that occurs due to the steel plates (needed to perform the momentum estimate) inevitably degrades the overall SPEC performance.

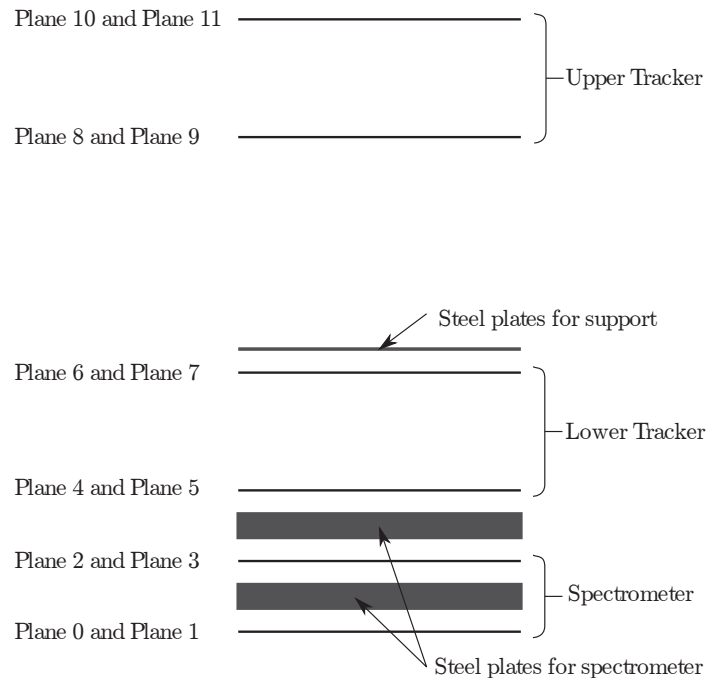


Figure 1: Simplified diagram of the CRIPT detector, showing only the position of the scintillator layers and steel plates (not to scale).

2 Data acquisition system performance

To receive the track information from the 24 PMTs, the CRIPT detector includes a custom data acquisition system (DAQ). Each PMT is read out by a dedicated Front-End (FE) board, which is, in-turn, controlled by a Collector card. The DAQ system includes 4 Collector cards: each detector section (UT, LT, SPEC) is controlled by a collector card that handles 8 FE cards, and the additional “master” collector coordinates the three “sub” collectors. The analog PMT signal is digitized by the FE board (when the pulse height exceeds a programmable threshold) and the pulse information is transmitted through the DAQ as an individual “packet”. Each FE board has 64 ADC (analog-to-digital converter) channels, which allows for every PMT channel (and therefore every scintillator bar) to have a dedicated, and individually programmable, data-path. Moreover, the DAQ system is responsible for combining all 1452 data-channels so that the read-out events are complete and understandable by back-end analysis routines. To accomplish this data-merging, the data-paths are multiplexed at several stages: 8 channels are merged at the ADC chip level; the data from the 8 chips are the multiplexed within the FE board before being sent to a sub-collector; the sub-collector then multiplexes data from 8 FE boards and sends it to the master-collectors; finally, the master-collector merges the data from the three sub-collectors and forwards it to the back-end computer (BEC) where it is recorded to disk.

Figure 2 shows a diagram of the DAQ architecture, highlighting the master-/sub- collector

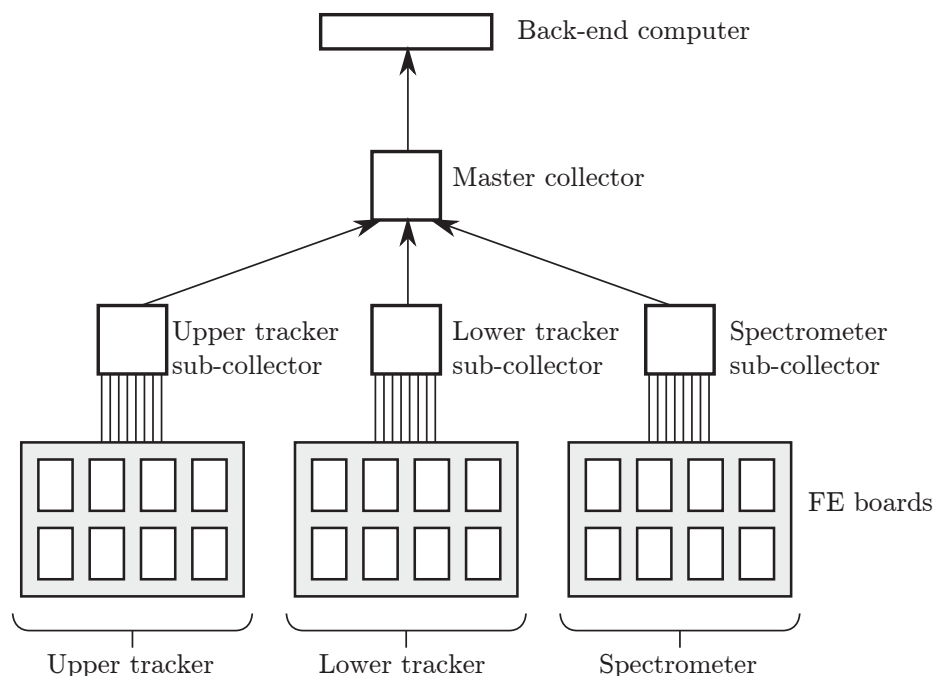


Figure 2: Simplified diagram of the DAQ architecture. The thin black lines represent the data-paths: the 24 FE boards are connected to 3 sub-collectors; the sub-collectors are connected to the master-collector; the master-collector is connected to the back-end computer.

distinction. It is important to understand the DAQ architecture to explain the operation of the DAQ event trigger. The event trigger is the condition that needs to be satisfied for detector data to be read out and recorded. Detector trigger conditions usually involve the time-wise coincidence of signals, which helps filter out detector noise. For the CRIPT detector the standard trigger condition requires a PMT pulse to be present in at least all of the UT and LT planes, which is the minimum condition to determine tracks through the UT and LT for imaging (note that PMT pulses in the SPEC layers can still be recorded, but they are not required to be present for this trigger). The enforcement of this trigger condition is accomplished in two stages: first, the sub-collectors enforce a sub-trigger within their detector sections, which involves having that sub-collector look for the coincidence of PMT pulses in all four planes of the detector section and only sending on those pulses in coincidence to the master collector. Next, the master-collector looks for the coincidence between the pulses arriving from the UT and LT, and will send to the BEC all packets within the coincidence window when the trigger condition is met.

However, it was noticed that not all of the events recorded by the DAQ appeared to satisfy the detector trigger condition. That is, for about 18% of the recorded detector events, at least one of the UT or LT planes would be totally empty of pulses. After investigation, it was determined that this was an issue stemming from limited bandwidth within the master-collector. In order to multiplex data-packets from up to eight inputs, each collector input

PMT Voltage (for the excluded plane)	P4	P5	P6	P7	P8	P9	P10	P11
800 V					407			
840 V	462	435	439	443	408	419	423	427
875 V	463	436	440	444	409	420	424	428
900 V	464	437	441	445	410	421	425	430
925 V	465	438	442	446	411	422	426	431
950 V					406			

Table 1: Data runs for high-voltage scan.

has in-memory first-in-first-out (FIFO) buffers to store the packets until it is their turn to be multiplexed. However, when too many packets arrive concurrently, the FIFO buffers can overflow causing data loss. Moreover, since a sub-collector will merge and send all of its data-packets to the same master-collector input, the master-collector FIFO buffers need to be significantly larger than the sub-collector buffers to accommodate all of the data-packets that arrive from that detector section. A firmware upgrade which quadrupled the FIFO buffer size helped significantly mitigate the packet-loss issue, such that after upgrade, only about 1% of events recorded do not satisfy the trigger condition. This improvement benefits the CRIPT analysis as a whole, as the result is an additional 17% of usable events for imaging, which will help decrease collection times, and improve image resolution.

3 PMT high-voltage scan

The PMT set-voltage is an important operating parameter, as it controls the gain of the PMT device: if the voltage is set too high, the signal pulse-heights will be larger than the dynamic range of the ADCs and charge information (used to improve the hit resolution) will be lost; if the PMT voltage is set too low, the pulse-heights will be too small to make accurate charge determinations (again affecting the hit resolution). Following this argument, there should be a set-voltage that optimizes the dynamic range of the ADCs – thereby minimizing the hit resolution.

A data series was collected to investigate the hit resolutions and efficiencies as a function of PMT set-voltage for each plane in the UT and LT. Each datarun taken focuses on one plane and one set-voltage (see Table 1). Only the set-voltages for two PMTs from the plane under investigation are changed. Moreover, the plane under investigation is removed from the event trigger to avoid trigger bias when measuring the plane hit efficiency.

3.1 Hit resolution

The hit resolution (that is, how close the hit measured by the scintillator bars comes to actual point that the muon traveled through the plane) is particularly important for the CRIPT detector, as the quality of the final reconstructed images is related to how well the muon tracks can be determined, which depends strongly on the hit resolution. As such, it is important to minimize the overall hit resolutions and throughout this report, the hit resolution is taken as the overriding figure of merit to optimize.

The method for determining the hit resolution, σ , is discussed in Reference [3]. To summarize, for a given event, two linear fits are performed on the measured hit positions for all planes for the coordinate (x or y) of the plane under study: the first fit includes all of the hits, the second fit includes all of the hits excluding those for the plane under study. Two histograms are then prepared for the sum of all events, where both histograms contain the residual values between the linear fit and the measured hit position for the plane under study and the linear fit (the first histogram contains all of the residual values for the linear fits including all hits, while the section histogram contains the residual values for the fits that excluded the hits from the plane under study). Gaussian fits are then performed on the two histograms, with the width of the distribution of residuals including all hits labeled as σ_w , and the width of the distribution excluding the hit from the plane under study labeled as σ_{wo} . The hit resolution is then estimated as:

$$\sigma = \sqrt{\sigma_w \sigma_{wo}}. \quad (1)$$

Note that this estimate relies on the assumptions that all the planes are the same and do not suffer from multiple scattering. For this study both assumptions are invalidated, as the planes do induce some small amount of multiple scattering, but more importantly, by changing the PMT set-voltage on only one plane, the plane-uniformity assumption is invalidated. For this reason, the resolutions determined from this study should not be considered as absolute, rather the optimization should be considered relative.

Figure 3a shows the measured resolution as a function of position across Plane 8 (the full set of UT and LT plots are included as Appendix B). The position-binning roughly corresponds to the scintillator bar width, which aids in the identification of problems affecting individual scintillator bars. Similarly, a plane-wise resolution value is determined from Fig. 3b, by histogramming all of the bin values from Fig. 3a, then performing a Gaussian fit. The mean of the Gaussian fit is taken as the aggregate hit resolution value for that plane and voltage. Finally, Fig. 3c shows the aggregate hit resolution values as a function of PMT set-voltage for plane 8 (the full set of UT and LT summary plots are included as Appendix A).

3.2 Efficiency

Another important performance indicator is the hit efficiency. A bar or plane with low hit efficiency (that is, where a hit should have been detected, but is not registered by the

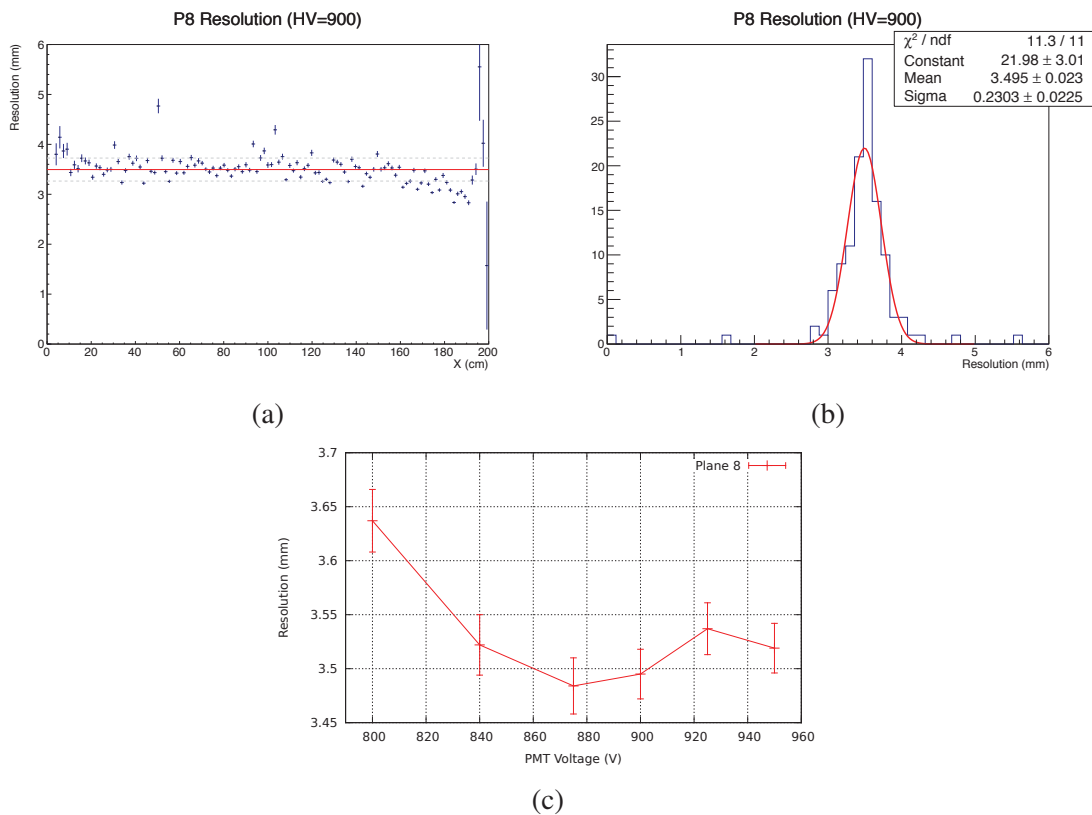


Figure 3: Resolution measurement for Plane 8: a) the hit resolution as a function of position along the plane, b) histogram of the measured resolution values, c) summary of measured hit resolutions as a function of PMT set-voltage.

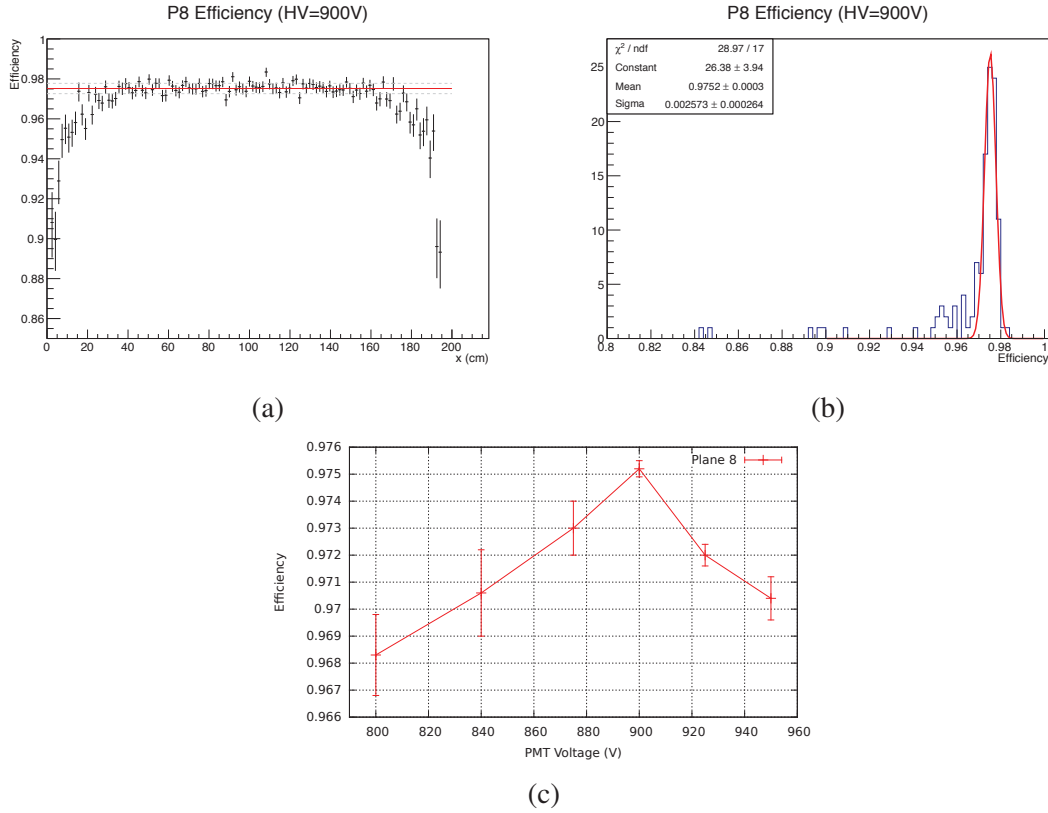


Figure 4: Efficiency measurement for Plane 8: a) the efficiency as a function of position along the plane, b) histogram of the measured efficiency values, c) summary of measured efficiency as a function of PMT set-voltage.

detector) can reduce the overall number of tracks detected (lengthening the track collection time required), or reduce the tracking effectiveness of regions of the detector. For these reasons, it is desirable to have the efficiency as close to 100% as possible.

For efficiency measurements, it is important that the plane under study is not included in the trigger condition. If the trigger strictly enforces that there should be a hit in a specific plane, it is difficult to look for missing hits in that same plane. For that reason, as detailed in Table 1, the plane under study was removed from the sub-collector trigger condition.

Moreover, for the efficiency analysis, two types of inefficiencies are considered: 1) when there are no hits registered at all in the plane under study, and 2) when there are hits in the plane under study, but those hits are nowhere close to where the track is passing through the plane. It should be noted that the packet-dropping issue described in Sec. 2 can contribute to inefficiencies recorded in this measurement (that is, a hit might be missing because the data-packet was dropped by the DAQ, rather than being due to a problem with the scintillator or PMT). However, with the DAQ improvements discussed in Sec. 2, this issue has a very small impact on the overall efficiency.

Threshold	50	60	70	80	90	100	110	120	130	140	150
Run	470	471	472	473	474	475	476	477	478	479	250

Table 2: List of dataruns for the threshold scan (PMT set-voltage 900V).

Figure 4a shows the efficiency estimate as a function of position across plane 8. Similar to Fig. 3a, the positional binning is on the order of the bar width so that problems with individual bars might be identified. A plane-wise efficiency value is determined in Fig. 4b (where the method for determining the overall efficiency value is identical to that of Fig. 3b). Finally, a summary of the efficiency measurements as a function of PMT set-voltage for plane 8 is given as Fig. 4c (the full set of UT and LT summary plots are included as Appendix A).

3.3 Recommendation

Although there is a fair bit of variability in the estimates, the results of the set-voltage scan (Appendices A and B) generally suggest that the optimal set-voltage is around 900V. For the CRIPT detector at around this voltage, the PMT pulse-height distributions fully utilizes the dynamic ADC range, without excessively exceeding the ADC range.

4 Threshold scan

Figure 5 shows an example PMT pulse-height distribution for a single scintillator bar, where the x-axis is in units of ADC bins. The large peak to the left of the distribution is attributed to spontaneously emitted photons from the wavelength-shifting fiber [4], while the rest of the distribution comes from the scintillator single produced by through-going cosmic ray muons. It is important to separate the signal from the noise by rejecting as many spurious noise pulses as possible, while not erroneously refusing too much of the actual scintillator signal. The ADC threshold allows us to set the ADC bin below which pulses are rejected (for example, in Fig. 5 the ADC threshold is set to 50, which can be seen in the sharp drop-on at the far left of the distribution).

For the determination of the optimal ADC threshold, all of the PMT set-voltages were fixed to 900V, and a series of data-runs taken with a variety of ADC thresholds. Table 2 gives the list of data-runs and their corresponding threshold values, which ranged from 50 to 150. Figure 6 summarizes all the plane resolution values as a function of ADC threshold.

4.1 Recommendation

From Fig. 6, the majority of planes see an resolution improvement as the ADC thresholds are increased from 50 to about 120. However, above a threshold of 120, the resolutions

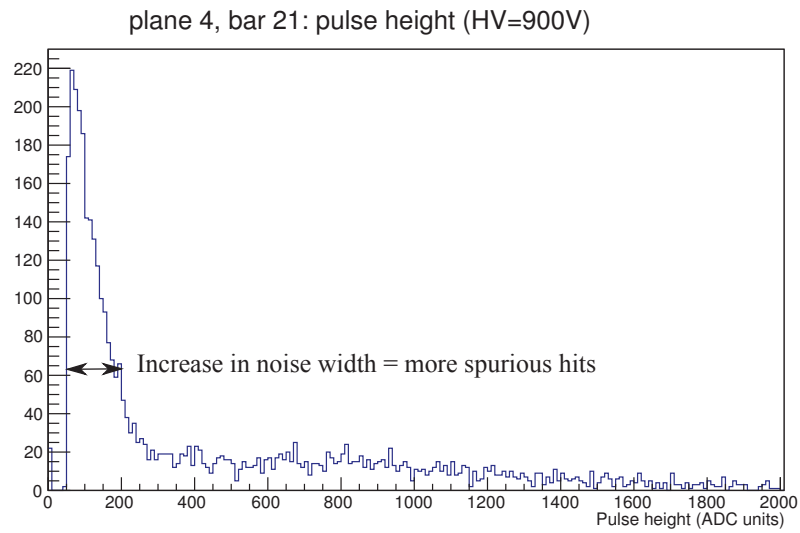


Figure 5: Pulse-height distribution for bar 21, plane 4 at PMT voltage 900V.

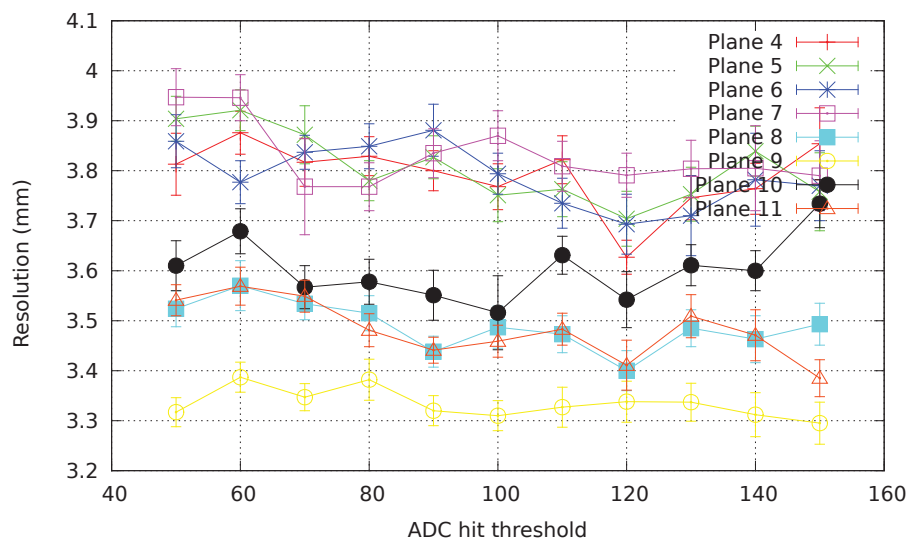


Figure 6: Plane resolutions as a function of ADC threshold for the Upper and Lower Trackers.

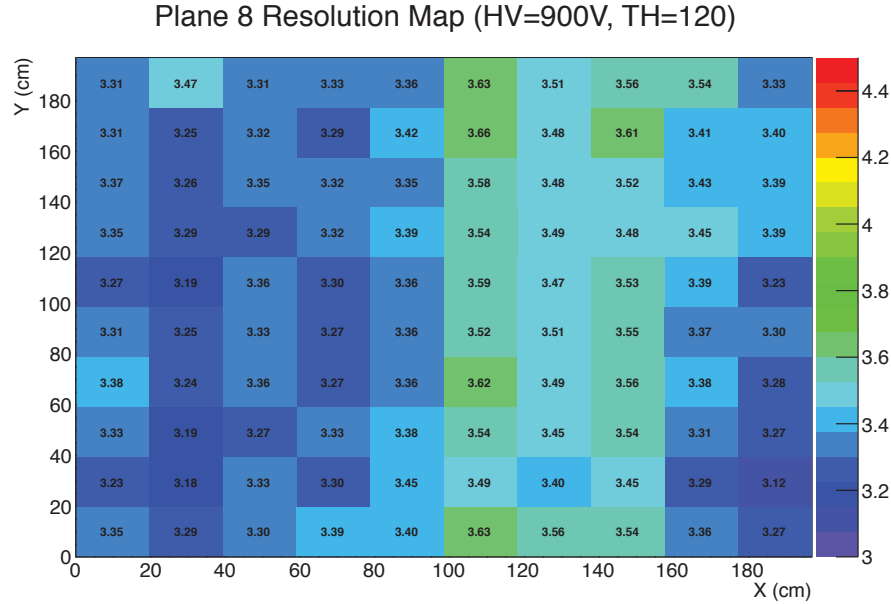


Figure 7: Resolution map for Plane 8

appear to worsen for most planes. For this reason, a threshold setting of 120 will likely provide the optimal hit resolution when the PMTs are set to 900V.

Once the operation parameters have been chosen, the a dataset using the ‘nominal’ settings can be collected to determine the baseline resolution. Figure 7 shows the measured hit resolution values binned across both x- and y-coordinates for plane 8. The poor resolution values between $100 \text{ cm} < x < 160 \text{ cm}$ is likely due to a poorly functioning bar in plane 10 (since hit information from plane 10 is also used for plane 8). The full set of resolution maps for the UT and LT is included as Appendix C.

5 Monte Carlo simulation

A powerful way to cross-check the results coming from a detector is to perform a Monte Carlo simulation. With such a simulation, the input (in this case, the trajectory and momentum of the through-going muon) is known and can be directly compared with the result after the simulated detector event has been processed by the analysis suite. For this study, a GEANT4 simulation was conducted in order to emulate cosmic ray muons passing through the CRIPT detector. A number of detector effects, such as light attenuation in the wavelength-shifting fiber and the quantum efficiency of the PMTs, are taken into account in an effort to keep the simulation as faithful to the actual data as possible. However, due mainly to time constraints, the implementation of a detailed geometry and the completion of a high-statistics simulation were infeasible. As such, this study focuses on the gross

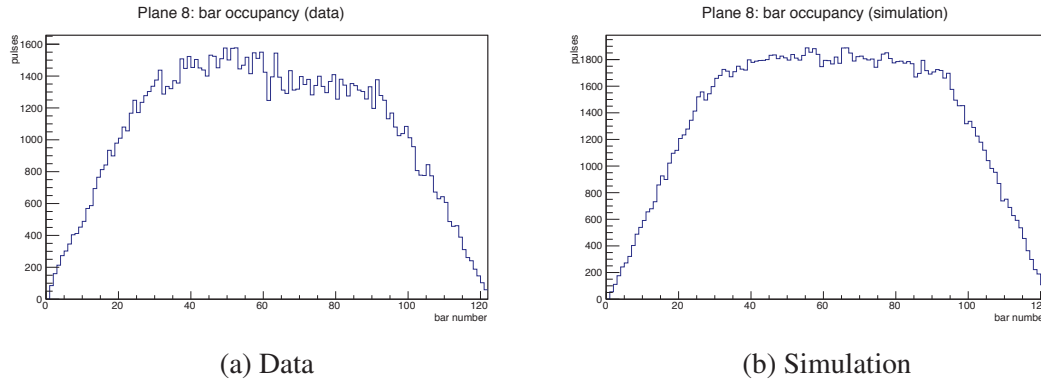


Figure 8: Comparison of bar occupancy distributions between data (a) and simulation (b) for plane 8.

aspects of the geometrical detector aspects and a rough validation of the muon momentum estimate implementation.

5.1 Geometric acceptance

Due to the geometry of the detector and implementation of the event read-out trigger, not every incoming cosmic ray muon trajectory will be recorded by the CRIPT detector. For example, incoming muons with track angles close to horizontal will not be able to pass through enough planes to satisfy the event trigger condition. It is important to understand the effect of the event trigger and detector geometry in order to properly interpret the data that are produced by CRIPT.

For this study, 400000 cosmic ray muons were simulated with (x,y) random positions just above the detector, and initial energies given by the CRY particle generator package [5]. Only events where the muon passed through all of the UT and LT planes were kept, resulting in a total of 96002 events. Figure 5.1 shows the comparison of bar occupancies (that is, how often the specific bar is included in a reconstructed track) between data and simulation for plane 8. As can be seen, both data and simulation share a very similar distribution shape, including the tapered edges and flat-top between bars 30 and 90 (the full set of UT and LT occupancy plots are included in Appendix D). The tapering in the occupancy distribution is an example of an acceptance effect, as the edge bars in plane 8 (as well as in planes 6,7, and 9) have a truncated distribution of track angles that can reach those edge bars and still result in a read-out trigger. As such, a change of read-out trigger, for example requiring hits in all twelve planes, would affect the shape of the resultant occupancy plots.

Similarly, the distributions of track angles reconstructed in the Upper and Lower Trackers and be compared with the simulation predictions. Figure 5.1 shows the zenith angle distribution in the x coordinate, for both the data and simulation. The spiky features in these

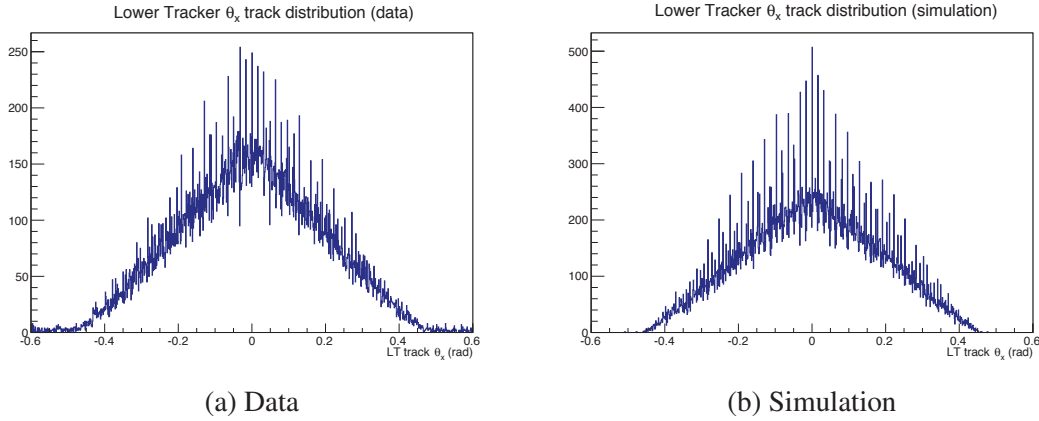


Figure 9: Comparison of θ_x distributions for reconstructed track angles between data (a) and simulation (b) for plane 8.

plots are due to tracks that only had isolated one-pulse hits. With the fixed positions of the bars, these tracks will be reconstructed at discrete angles, resulting in that sub-category of tracks to all be forced into the same angular bin. The overall shape and extent of the distributions is again due to the geometric acceptance of the detector. As can be seen from Figs. and , there are no gross defects found between these comparisons of the expected and observed distributions.

5.2 Momentum estimate

A novel aspect of the CRIPT detector is the inclusion of a spectrometer to estimate the momentum of the through-going cosmic ray muons. This spectrometer relies on two thick steel plates to introduce a measurable amount of multiple-scattering, and the particle momentum can then be inferred from that scattering [6]. The momentum information will then be used to improve the reconstructed images. It is therefore important to ensure that the momentum estimate is functioning correctly. A good method for validating the momentum estimates is to use the Monte Carlo simulation to compare the estimated muon momentum with the momentum known from the simulation input.

Figure 10 shows the correspondence between the simulated and reconstructed momenta for the 400000 event dataset described above (note the log scale for the colour scale). Only events where all twelve planes recorded hits (58363 events in total) are passed to the momentum estimate, and 15017 of those events (or 25.7%) successfully returned a momentum estimate. There is a obvious proportionality between the simulated and reconstructed momenta with a correlation factor of 0.425, although the estimated reconstructed momenta appears to be biased towards higher momenta. Likewise, Fig. 11a shows a histogram of the percent difference between the simulated and reconstructed momenta. Although the

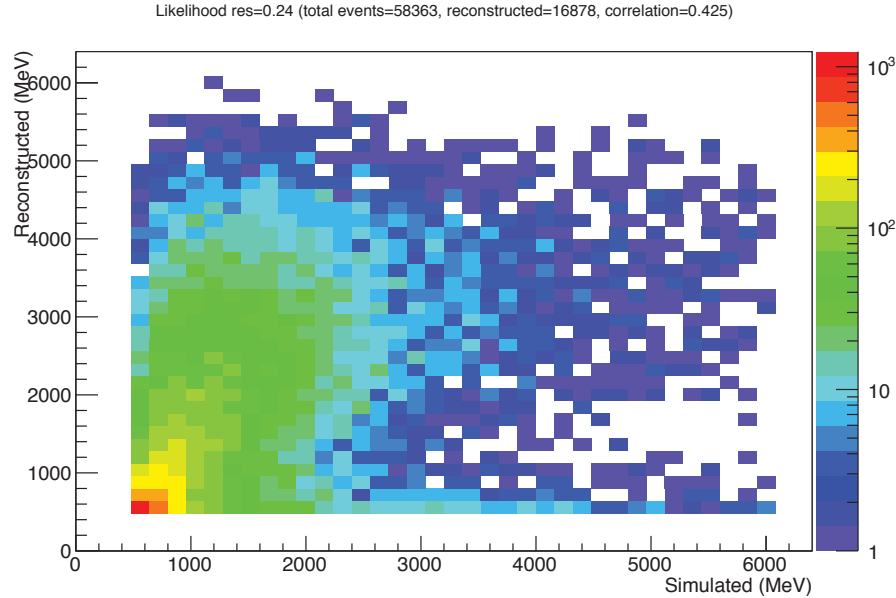


Figure 10: Comparison between the simulated and reconstructed muon momentum (note the log colour scale).

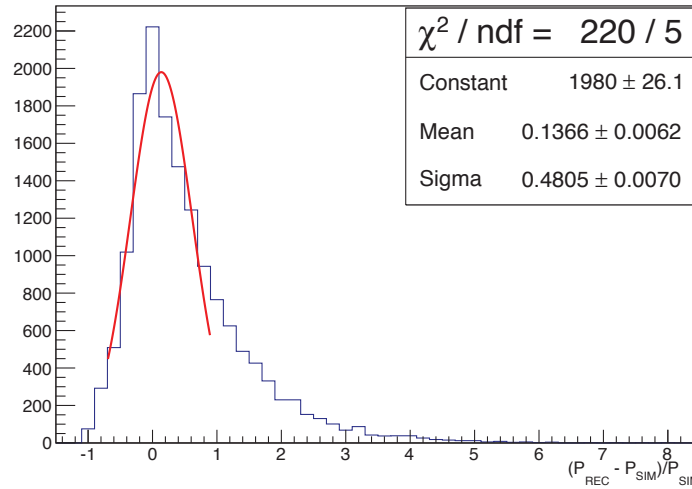
Gaussian in Fig. 11a does not provide a very good fit, it does give a rough estimate of about 48% for the reconstructed momentum resolution.

Finally, it is also interesting to investigate the performance of the momentum estimate as a function of simulated momentum. Figure 11b shows percentage of events that return momentum estimates as a function of simulated momentum. Above about 1 GeV, the number of events that successful return a momentum estimate drops off sharply. This is the expected performance of the reconstruction algorithm, as the multiple-scattering of high-momentum muons is not as pronounced as low-energy scattering and it can be difficult to accurately measure the scattering angles.

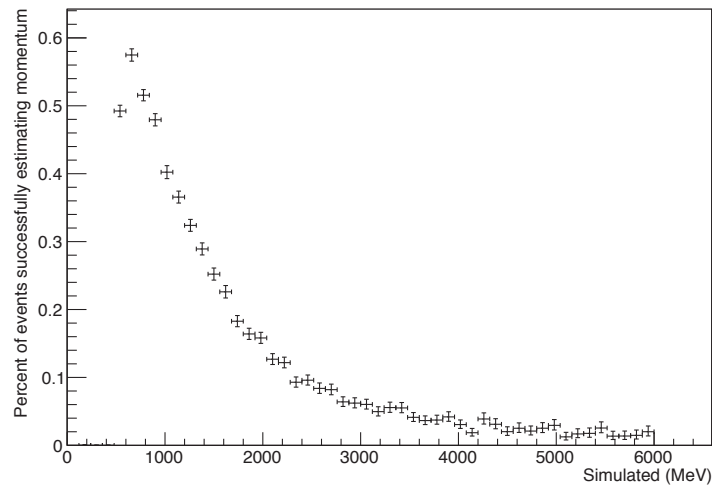
6 Conclusion

This study primarily investigated the optimal operating parameters for the CRIPT detector. Guided mainly by the goal of minimizing the hit resolution, it is determined that the PMT set-voltage of 900V and ADC threshold of 50 provide the optimal performance.

Secondly, a simple Monte Carlo simulation study was performed to investigate the geometric acceptance of the CRIPT detector and to validate the momentum estimate implementation. In both cases, the detector and the analysis algorithms were found to perform as expected.



(a) Percent difference between the simulated and reconstructed momenta. The Gaussian fit roughly estimates the reconstructed momentum resolution.



(b) Performance of the reconstructed momentum estimate as a function of simulated particle momentum.

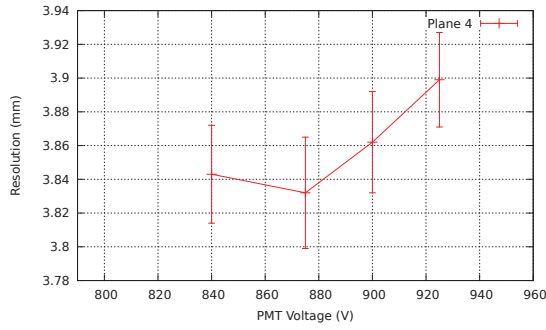
Figure 11: Reconstructed muon momentum estimate performance.

References

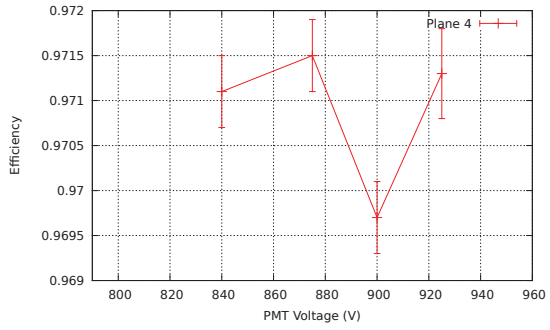
- [1] Waller, D. (2010), A simulation study of the Cosmic Ray Inspection and Passive Tomography (CRIPT) muon spectrometer, (DRDC Ottawa TM 2010-168) Defence R&D Canada – Ottawa.
- [2] Waller, D. (2010), A simulation study of material discrimination using muon scattering tomography, (DRDC Ottawa TM 2010-211) Defence R&D Canada – Ottawa.
- [3] Boudjemline, K. (2012), Data analysis status, Carleton University.
- [4] Avvakumov, S., Barrett, W., Belias, T., Bower, C., Erwin, A., Kordosky, M., Lang, K., Lee, R., Liu, J., Miller, W., Mualem, L., Nichol, R., Nelson, J., Pearce, G., Proga, M., Rebel, B., Ruddick, K., Smith, C., Thomas, J., Vahle, P., and Webb, R. (2005), Spontaneous light emission from fibers in MINOS, *Nuclear Instruments and Methods in Physics Research A*, 545, 145–155.
- [5] Haggmann, C., Lange, D., and Wright, D. (2007), Cosmic-ray shower generator (CRY) for Monte Carlo transport codes, In *Nuclear Science Symposium Conference Record, 2007. NSS '07. IEEE*, Vol. 2, pp. 1143–1146.
- [6] Drouin, P.-L. and Waller, D. (2011), Muon momentum reconstruction algorithms for the CRIPT spectrometer, (DRDC Ottawa TM 2011-210) Defence R&D Canada – Ottawa.

This page intentionally left blank.

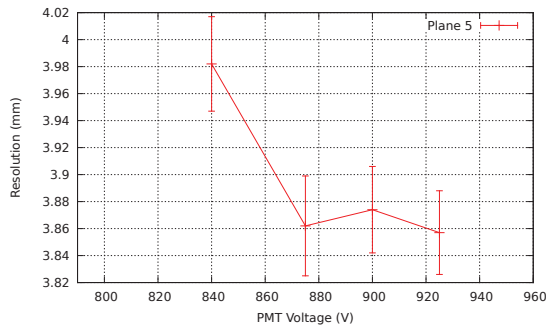
Annex A: Resolution and efficiency summary plots



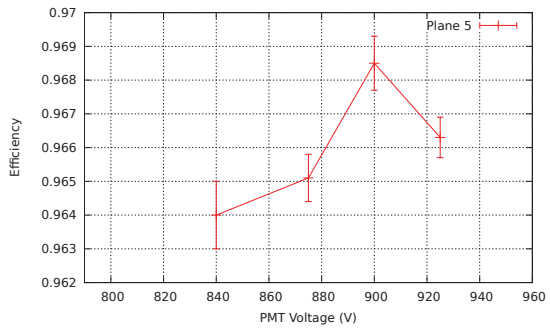
(a) Plane 4 resolutions



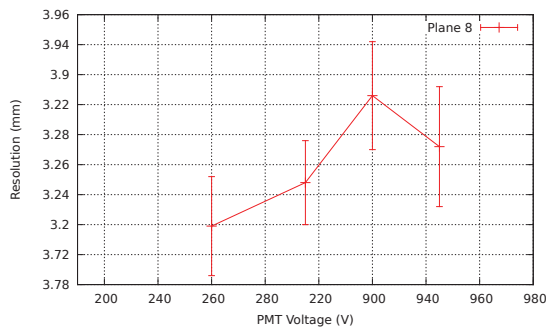
(b) Plane 4 efficiencies



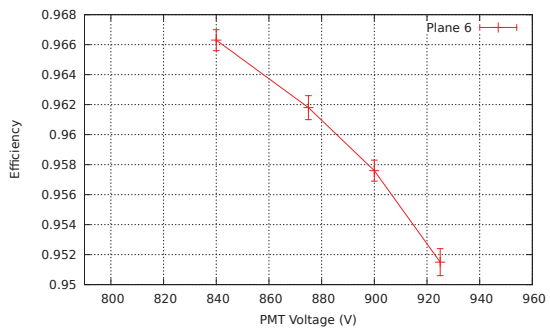
(c) Plane 5 resolutions



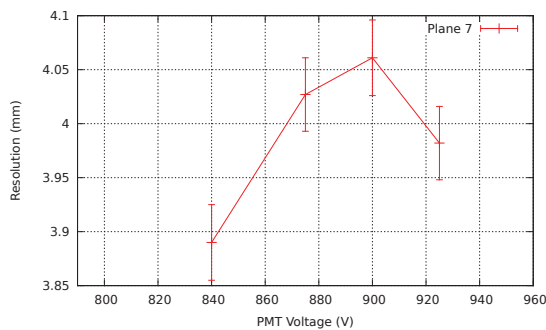
(d) Plane 5 efficiencies



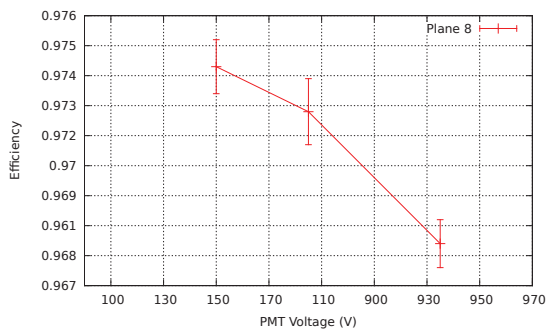
(e) Plane 6 resolutions



(f) Plane 6 efficiencies

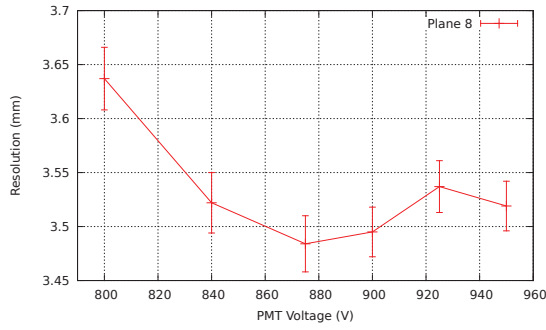


(g) Plane 7 resolutions

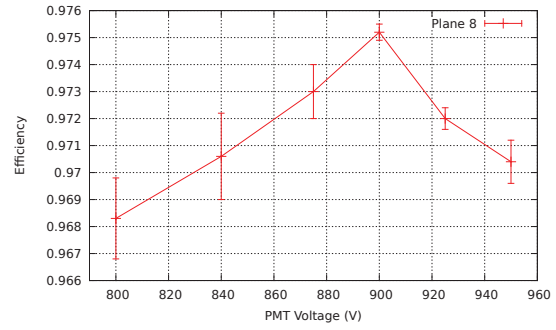


(h) Plane 7 efficiencies

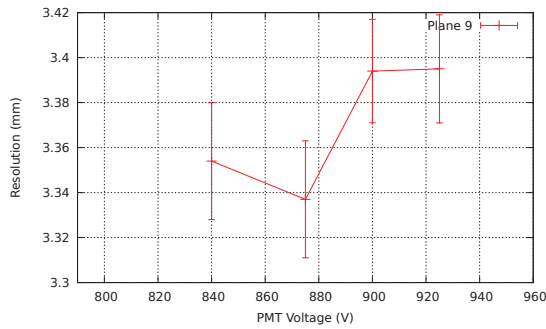
Figure A.1: Summary plots of resolutions and efficiencies as a function of set-voltage for the Lower Tracker.



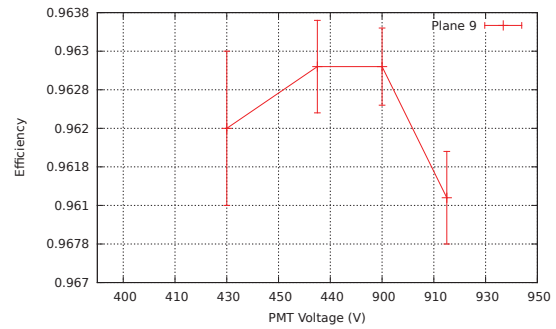
(a) Plane 8 resolutions



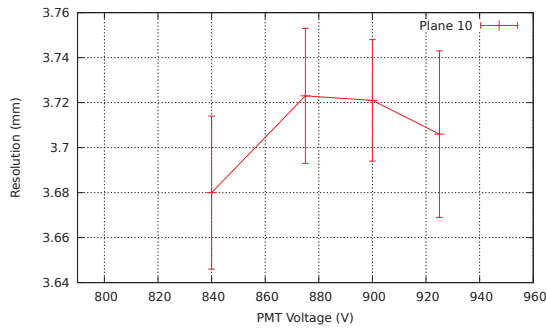
(b) Plane 8 efficiencies



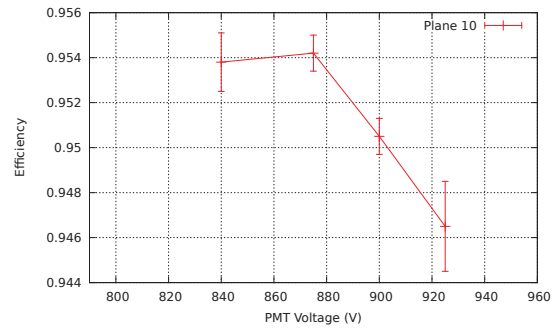
(c) Plane 9 resolutions



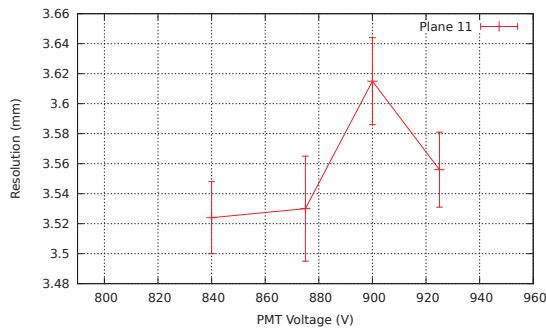
(d) Plane 9 efficiencies



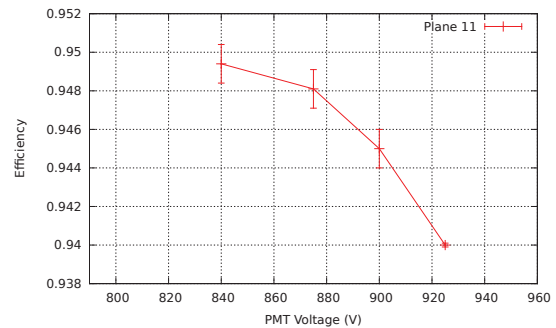
(e) Plane 10 resolutions



(f) Plane 10 efficiencies



(g) Plane 11 resolutions

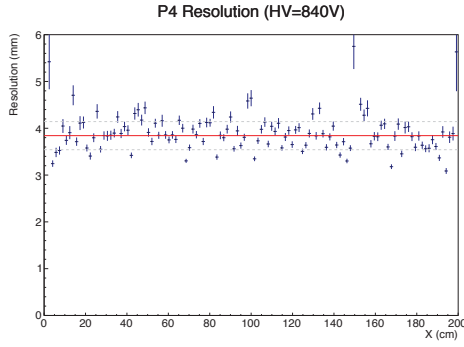


(h) Plane 11 efficiencies

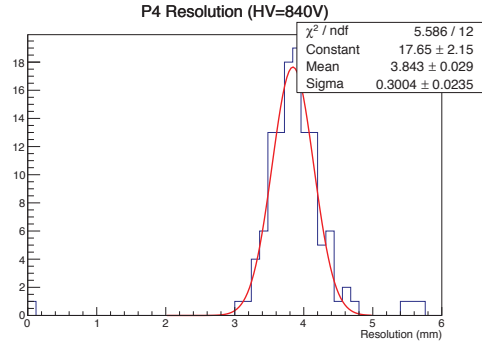
Figure A.2: Summary plots of resolutions and efficiencies as a function of set-voltage for the Upper Tracker.

This page intentionally left blank.

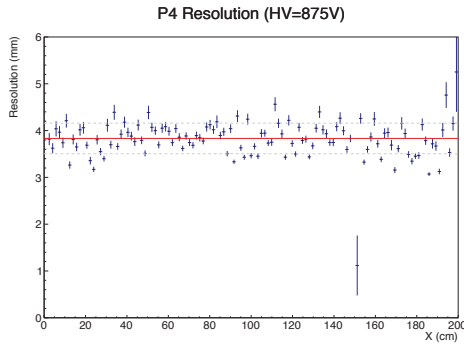
Annex B: Resolution and efficiency plots as a function of voltage



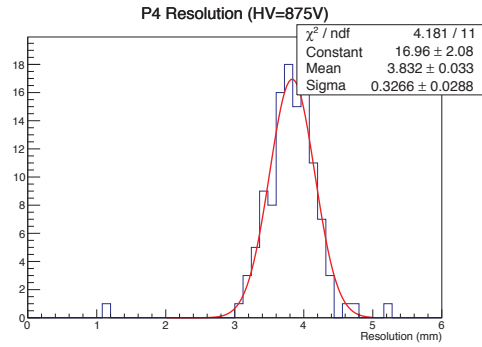
(a)



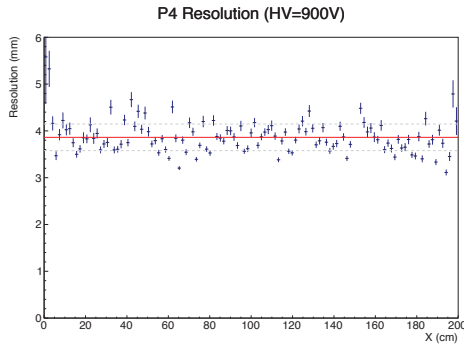
(b)



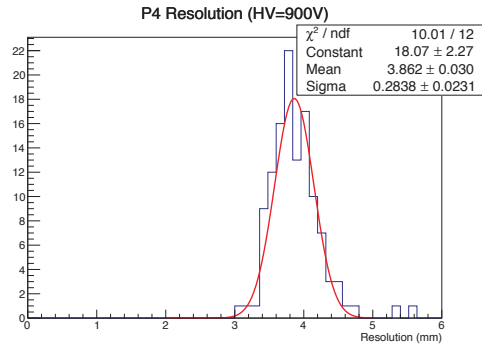
(c)



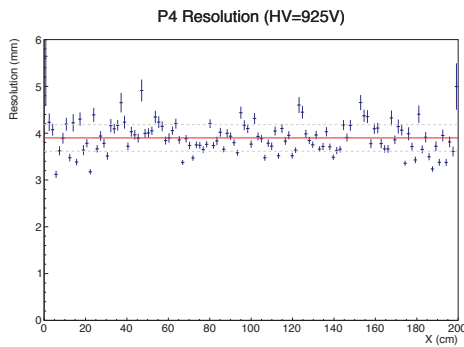
(d)



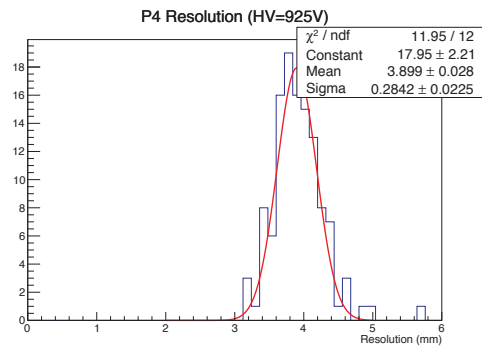
(e)



(f)

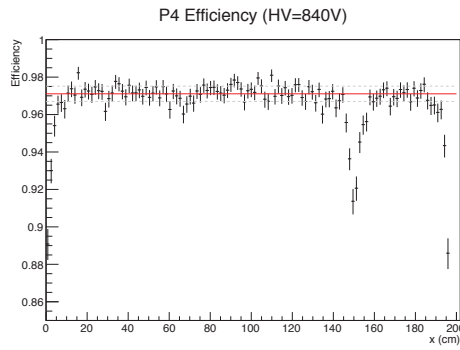


(g)

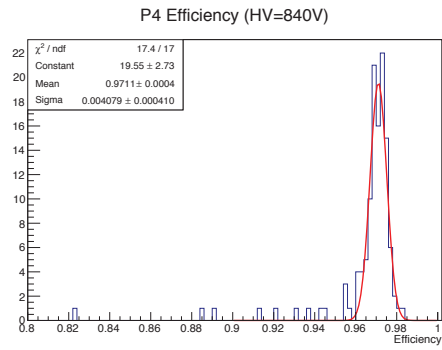


(h)

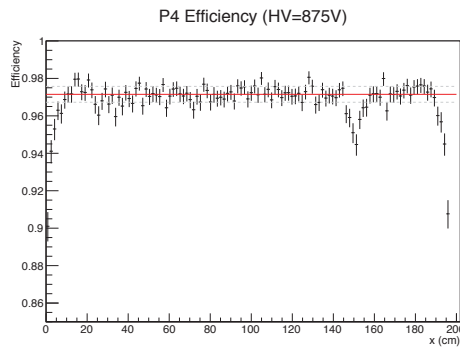
Figure B.1: Resolution measurements for Plane 4



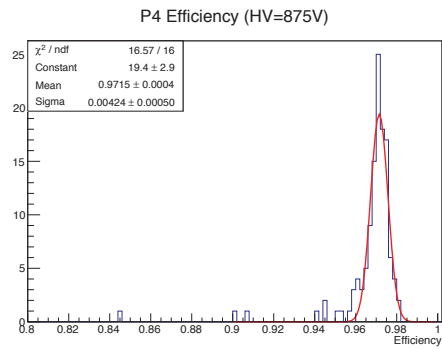
(a)



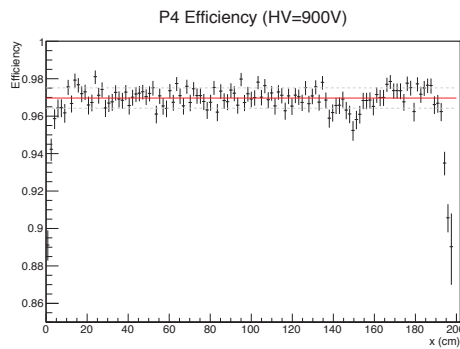
(b)



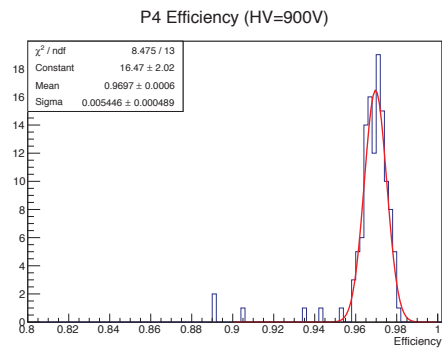
(c)



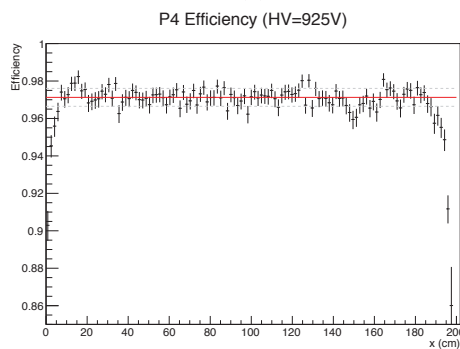
(d)



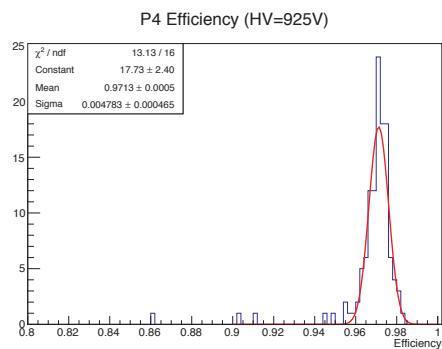
(e)



(f)

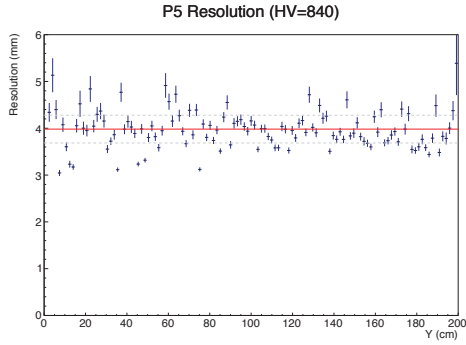


(g)

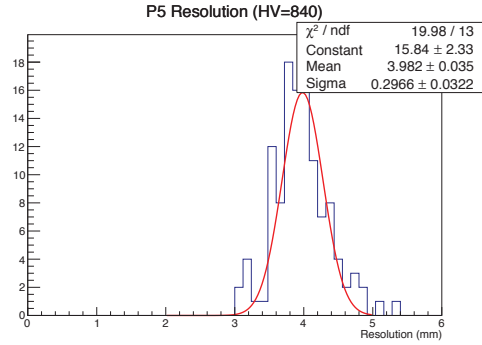


(h)

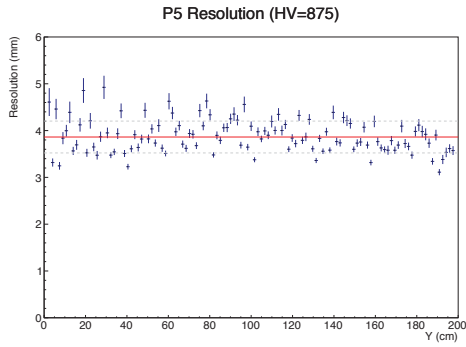
Figure B.2: Efficiency measurements for Plane 4



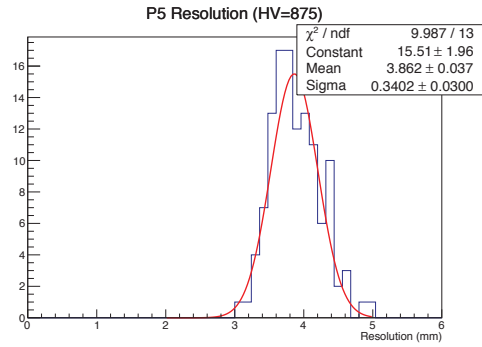
(a)



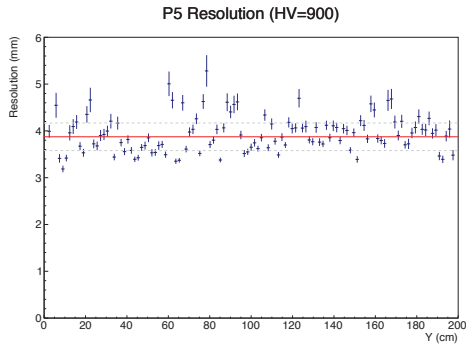
(b)



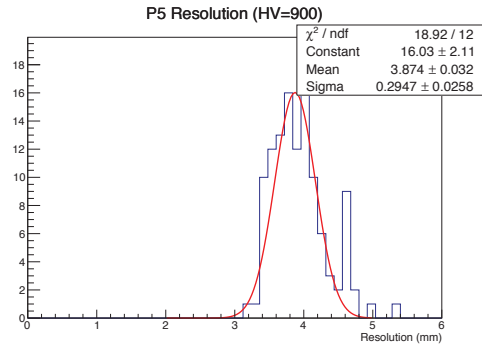
(c)



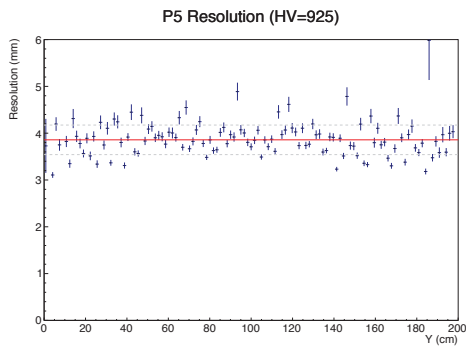
(d)



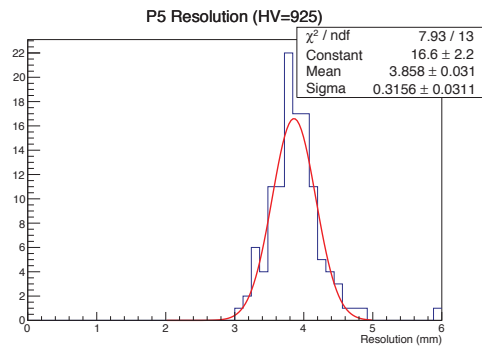
(e)



(f)

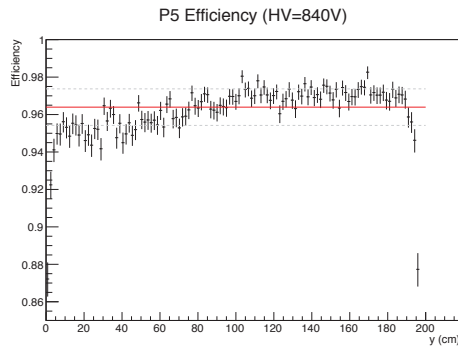


(g)

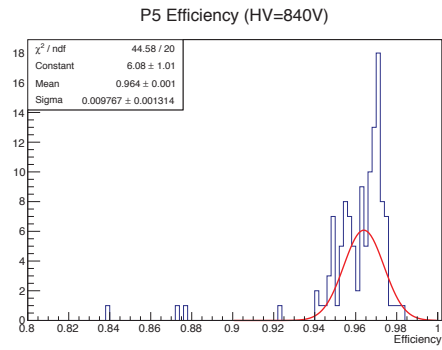


(h)

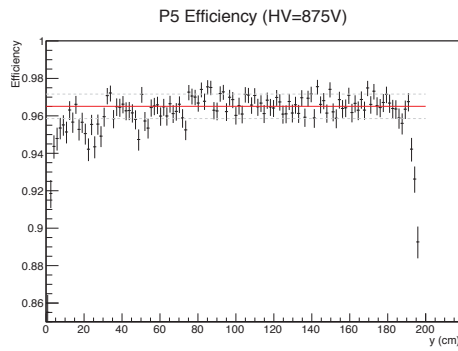
Figure B.3: Resolution measurements for Plane 5



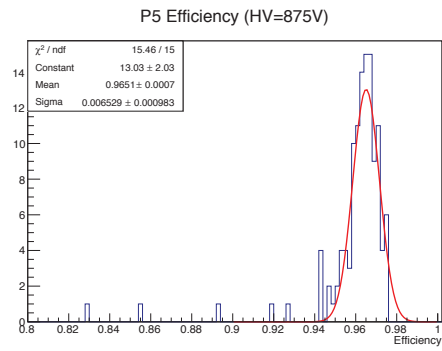
(a)



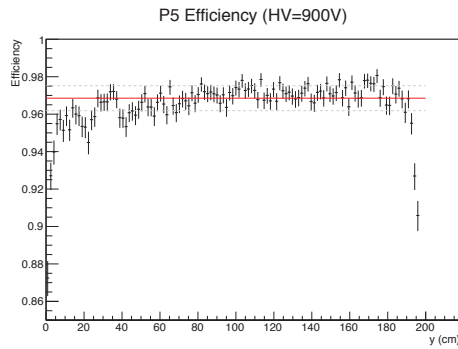
(b)



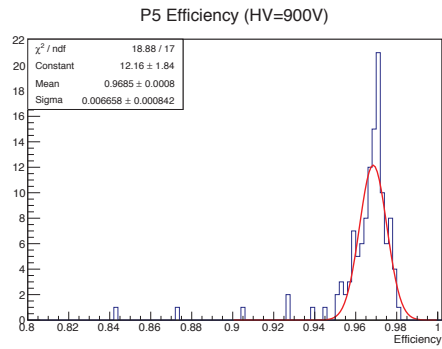
(c)



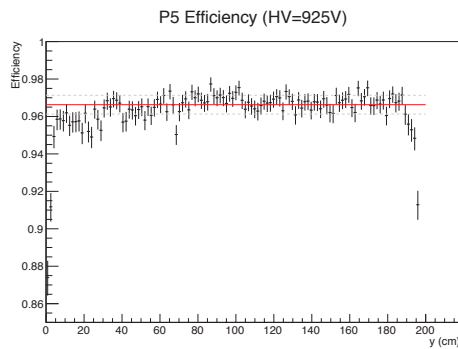
(d)



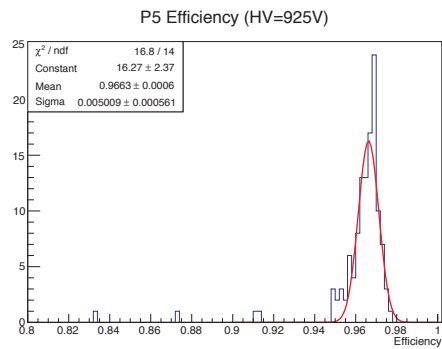
(e)



(f)

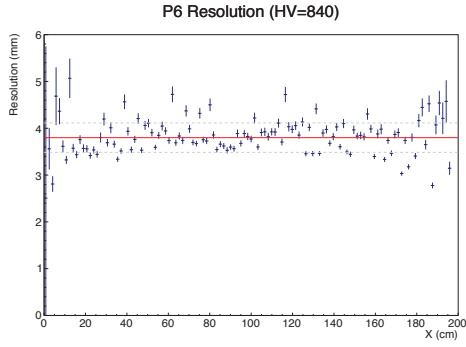


(g)

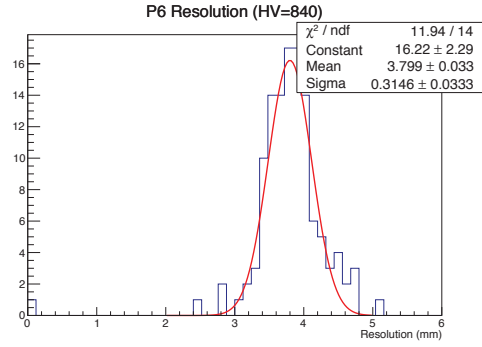


(h)

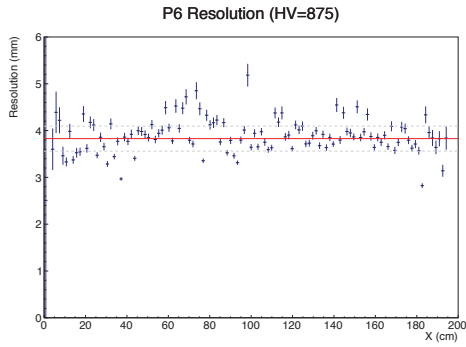
Figure B.4: Efficiency measurements for Plane 5



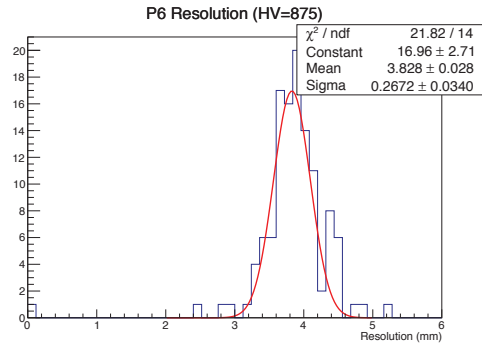
(a)



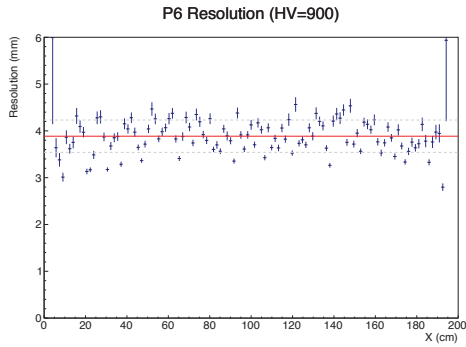
(b)



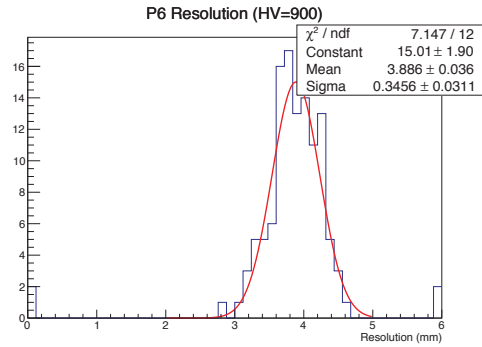
(c)



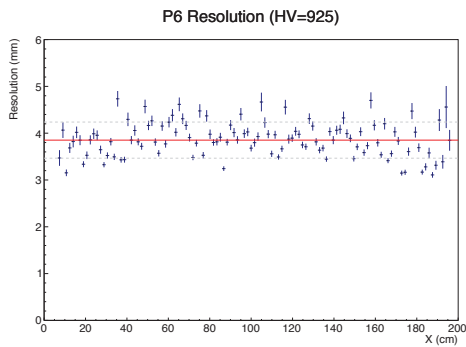
(d)



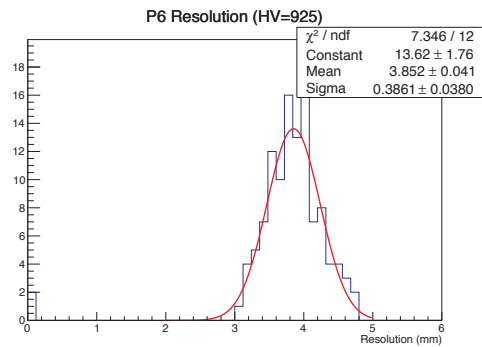
(e)



(f)

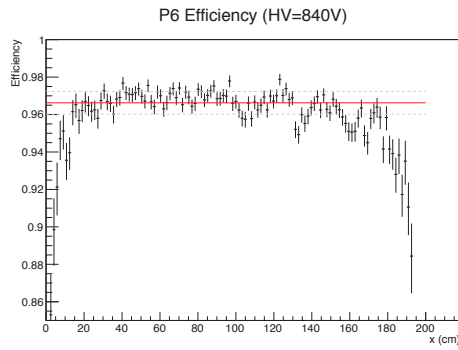


(g)

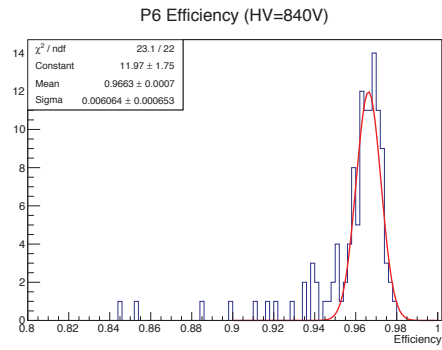


(h)

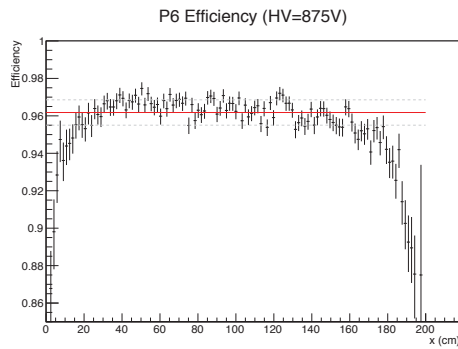
Figure B.5: Resolution measurements for Plane 6



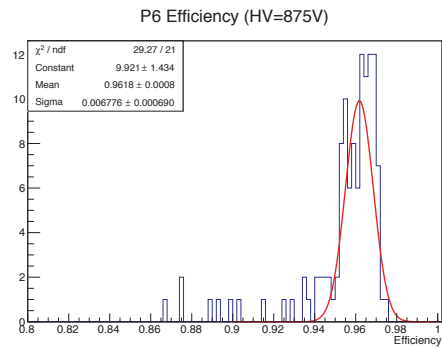
(a)



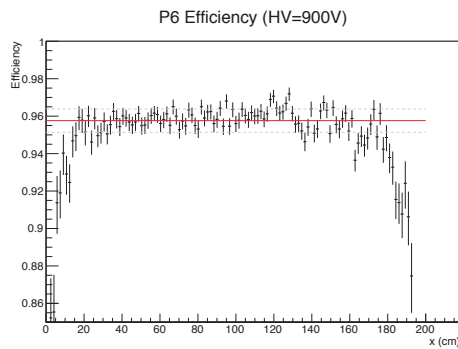
(b)



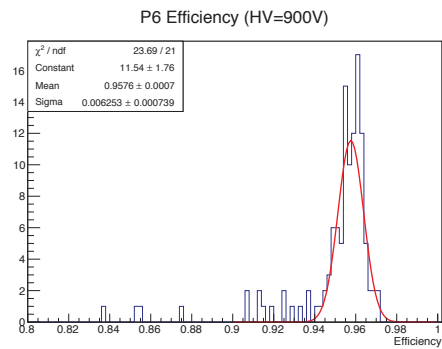
(c)



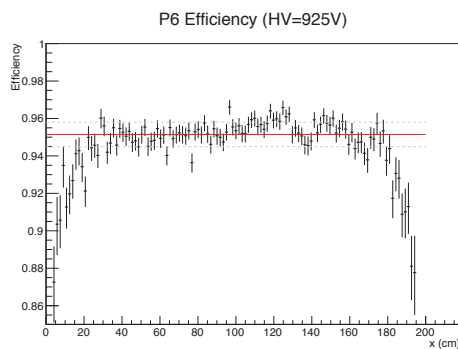
(d)



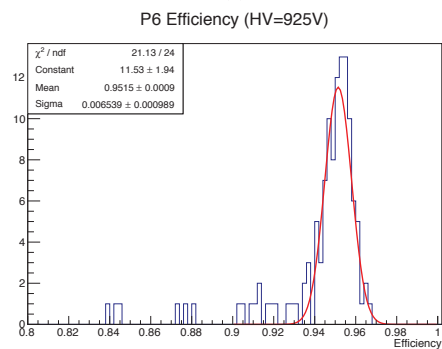
(e)



(f)

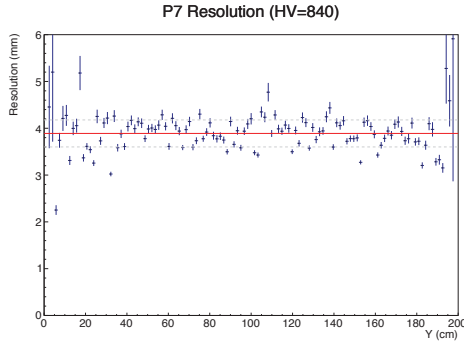


(g)

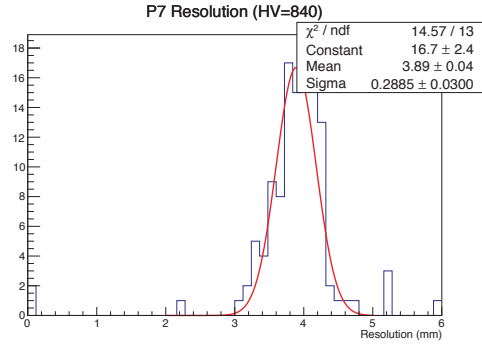


(h)

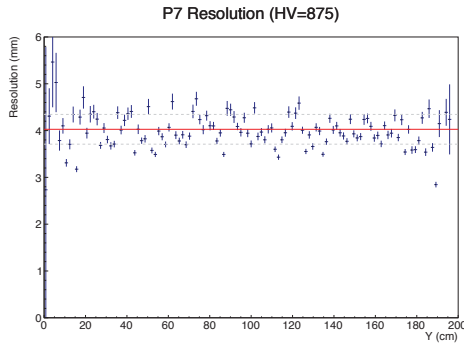
Figure B.6: Efficiency measurements for Plane 6



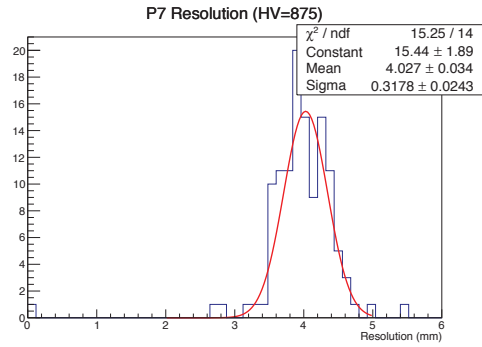
(a)



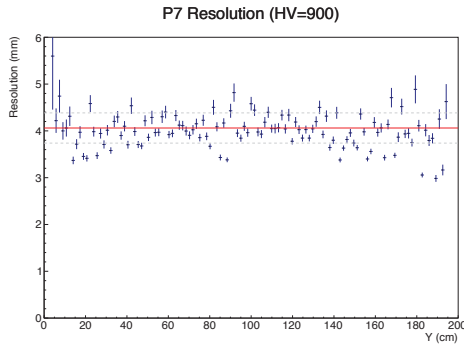
(b)



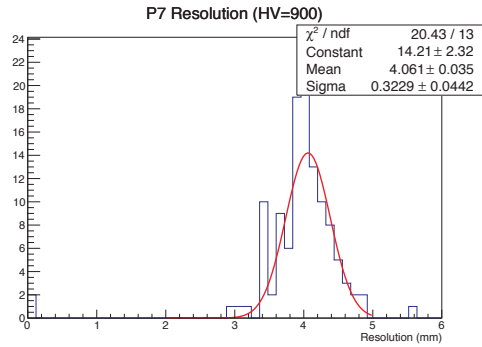
(c)



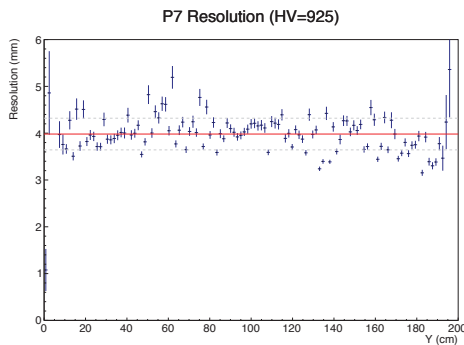
(d)



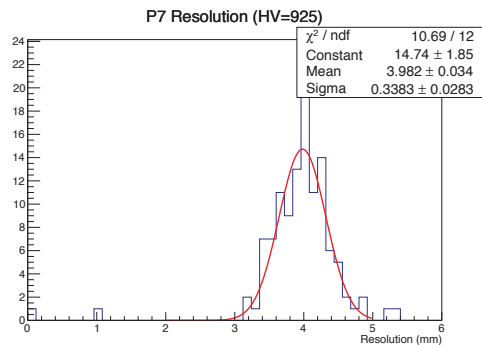
(e)



(f)

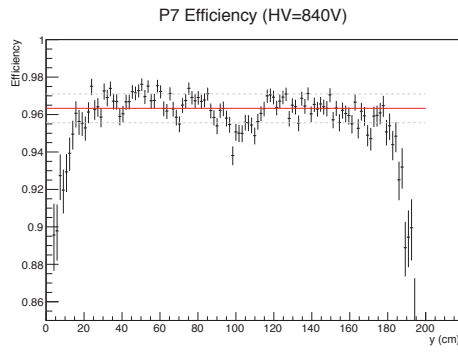


(g)

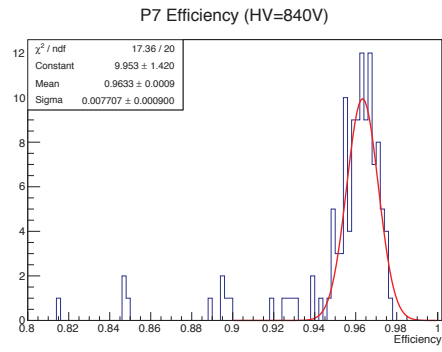


(h)

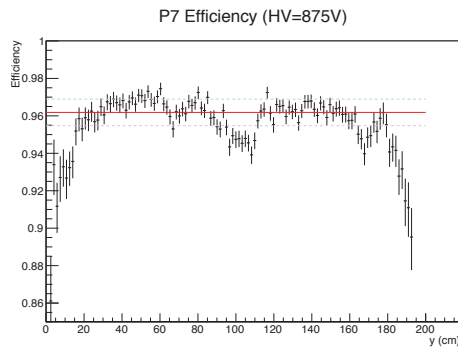
Figure B.7: Resolution measurements for Plane 7



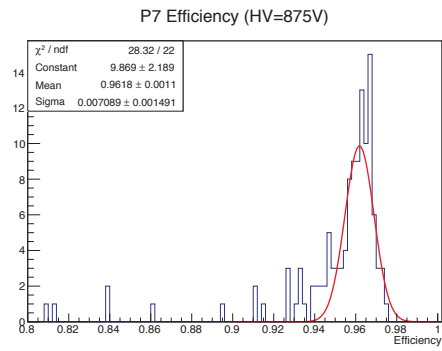
(a)



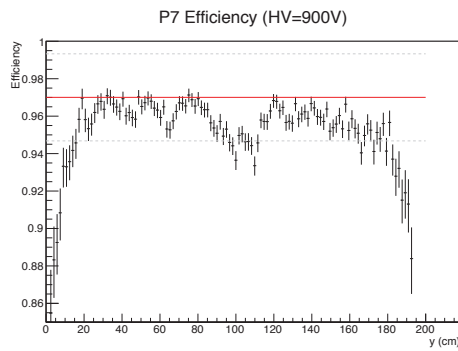
(b)



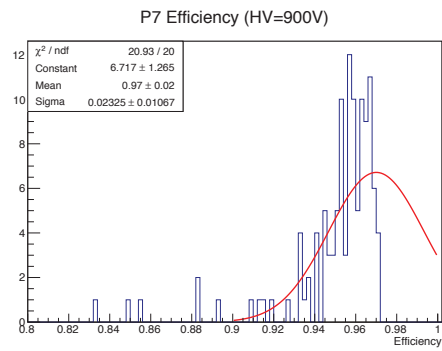
(c)



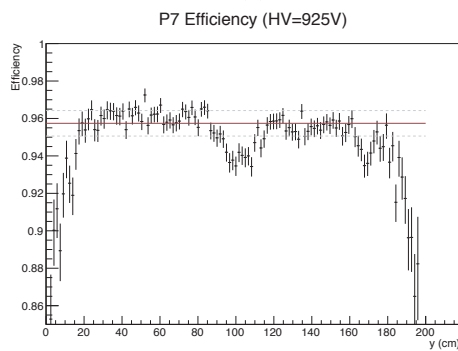
(d)



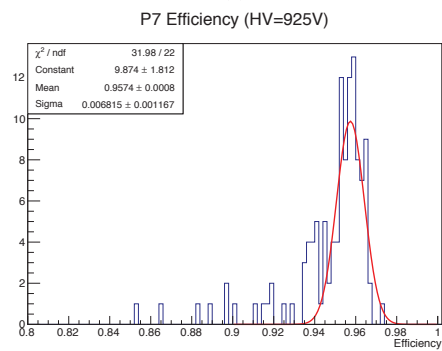
(e)



(f)

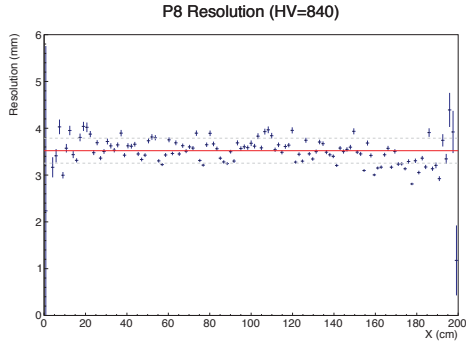


(g)

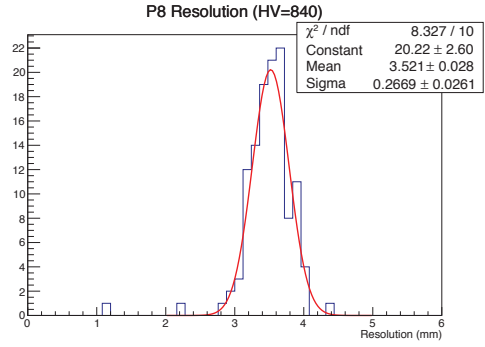


(h)

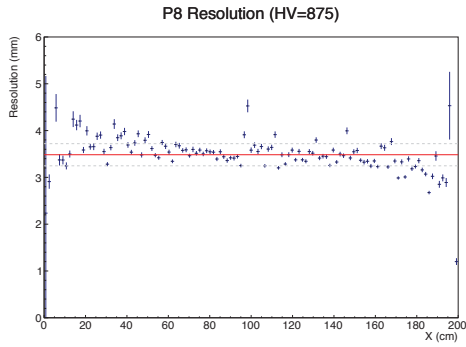
Figure B.8: Efficiency measurements for Plane 7



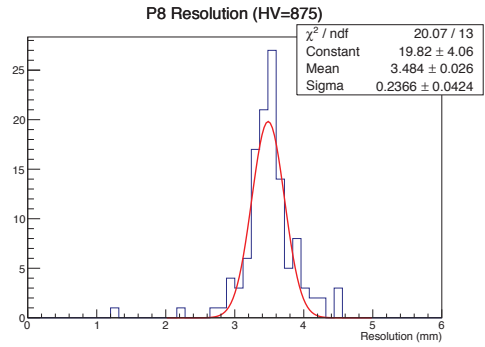
(a)



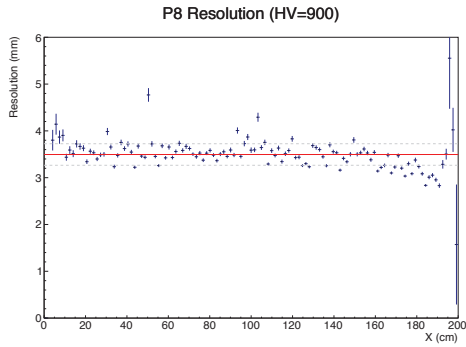
(b)



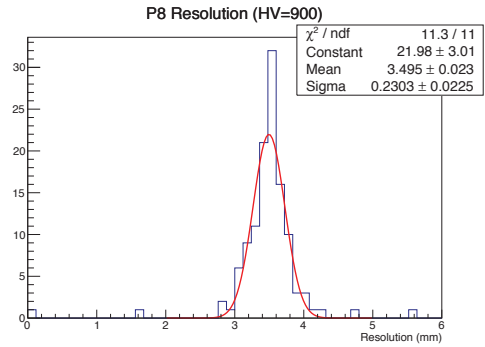
(c)



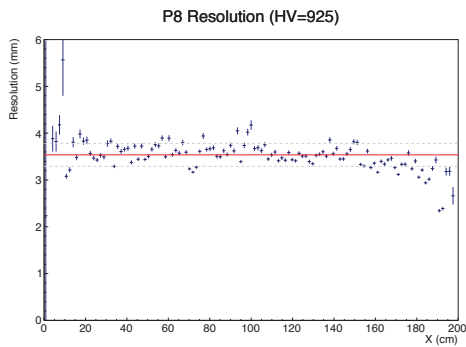
(d)



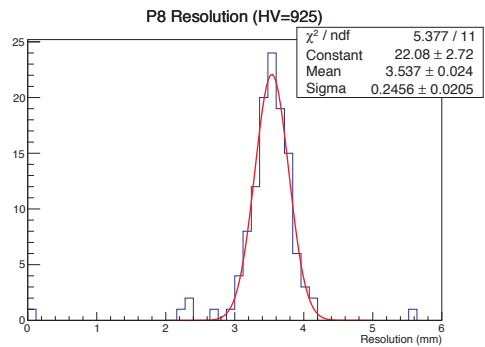
(e)



(f)

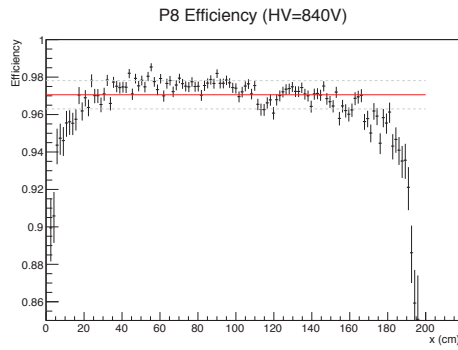


(g)

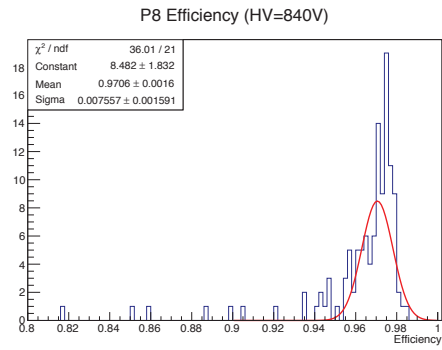


(h)

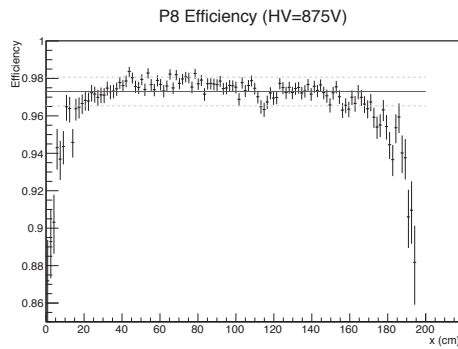
Figure B.9: Resolution measurements for Plane 8



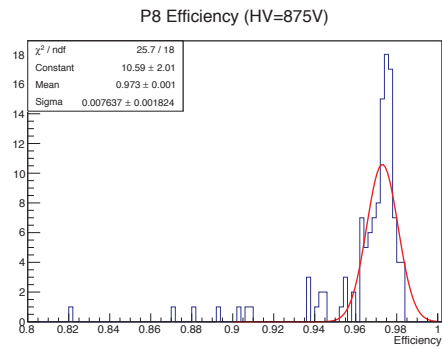
(a)



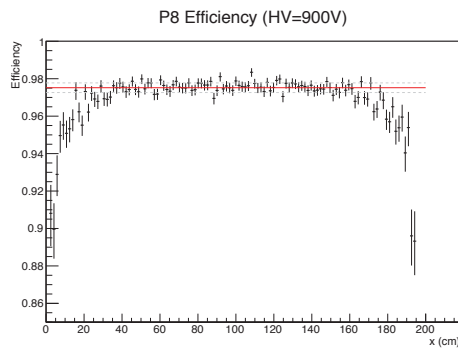
(b)



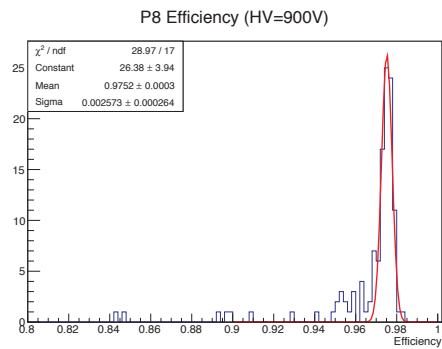
(c)



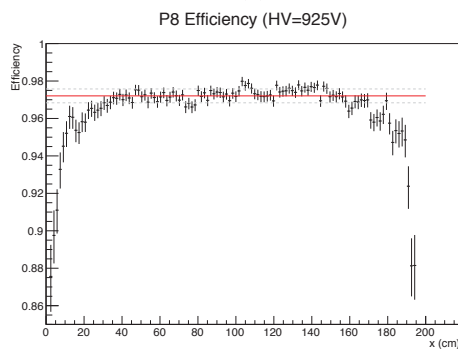
(d)



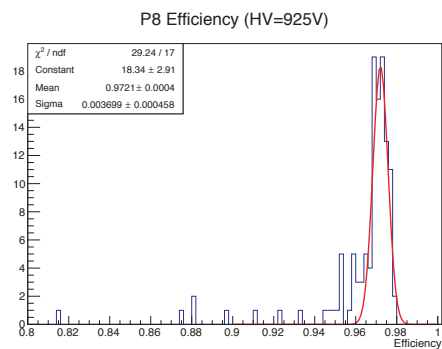
(e)



(f)

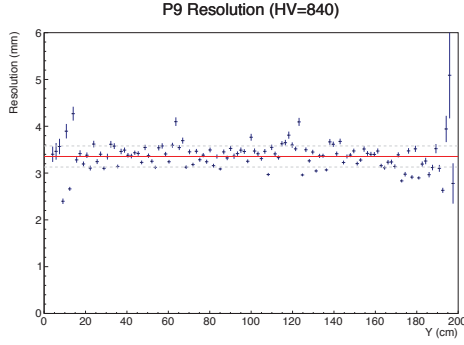


(g)

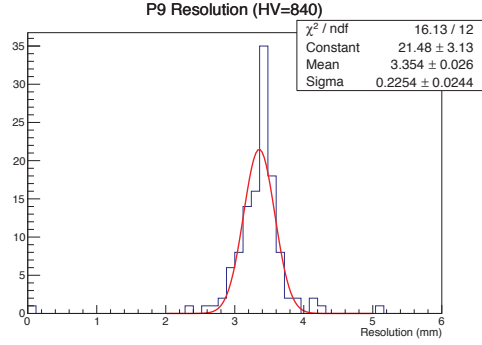


(h)

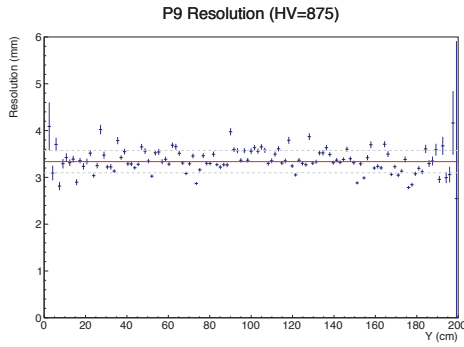
Figure B.10: Efficiency measurements for Plane 8



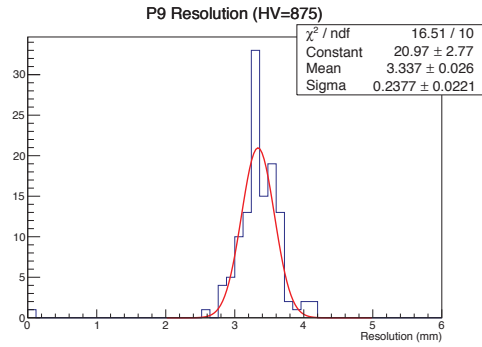
(a)



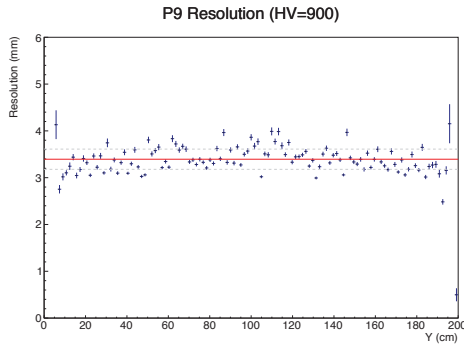
(b)



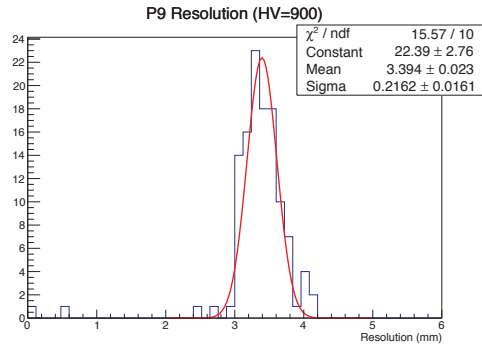
(c)



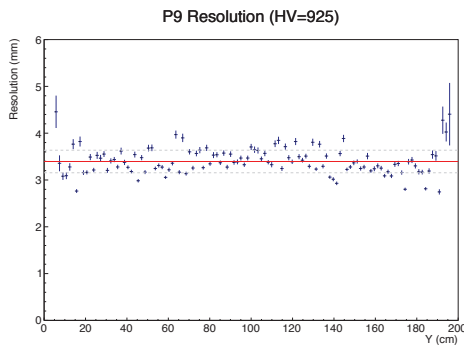
(d)



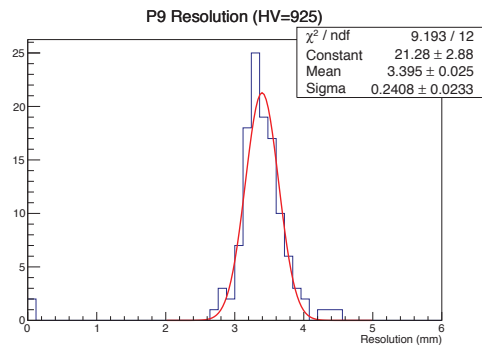
(e)



(f)

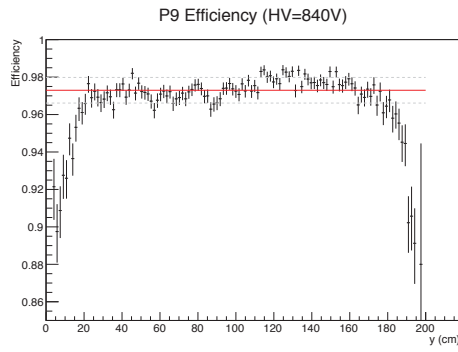


(g)

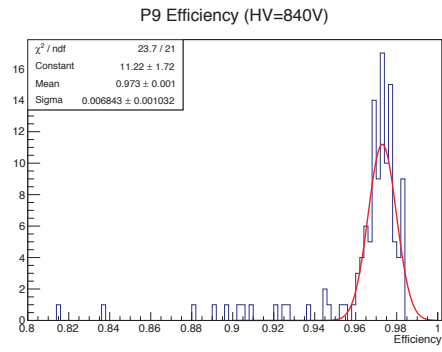


(h)

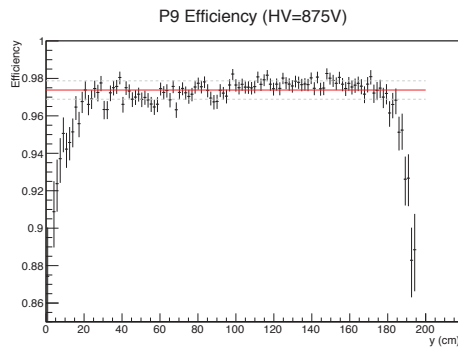
Figure B.11: Resolution measurements for Plane 9



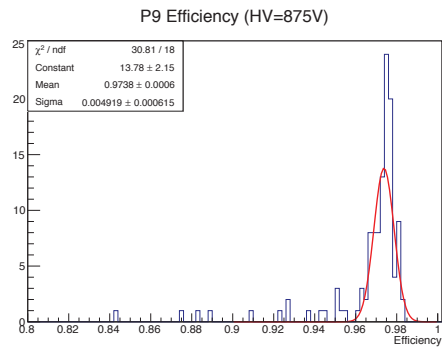
(a)



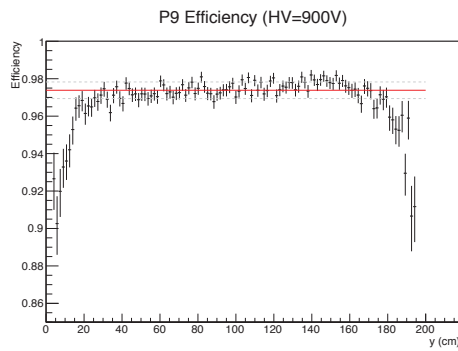
(b)



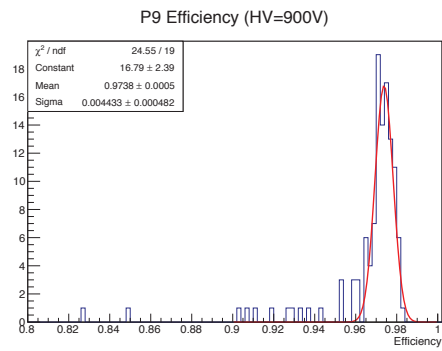
(c)



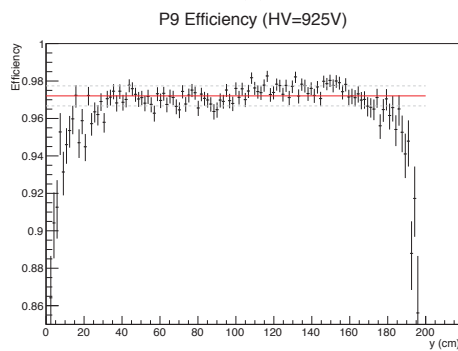
(d)



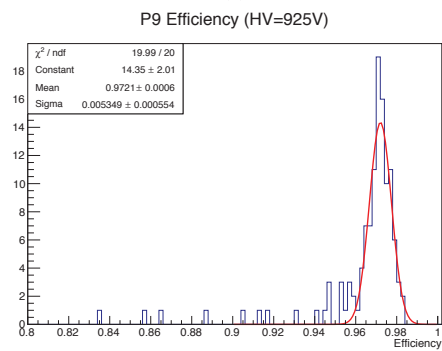
(e)



(f)

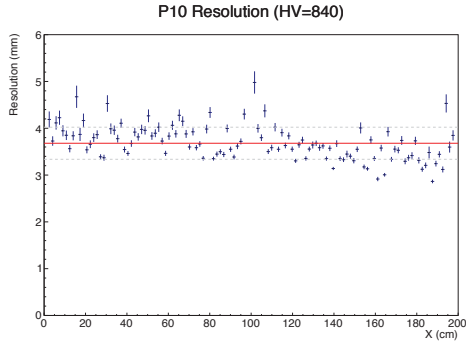


(g)

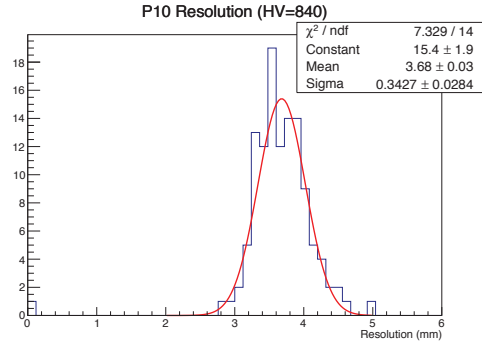


(h)

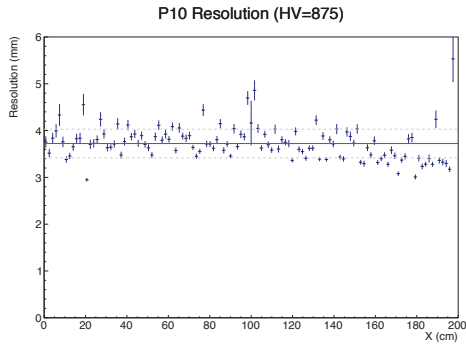
Figure B.12: Efficiency measurements for Plane 9



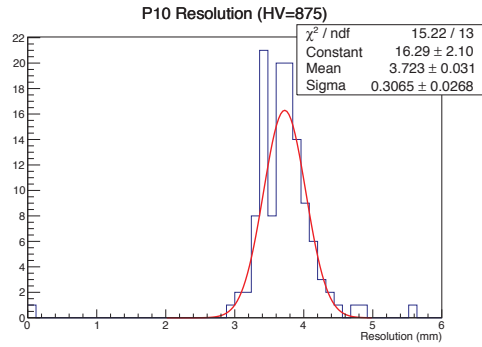
(a)



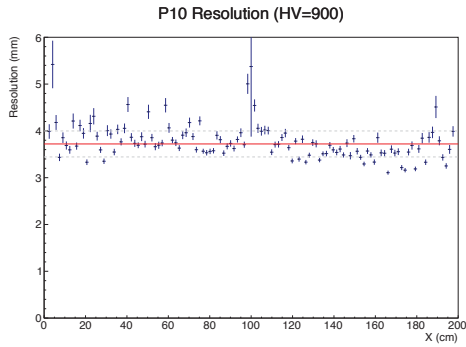
(b)



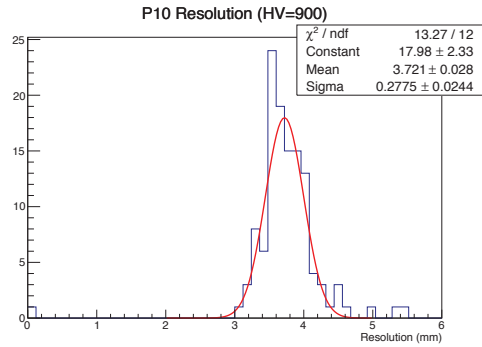
(c)



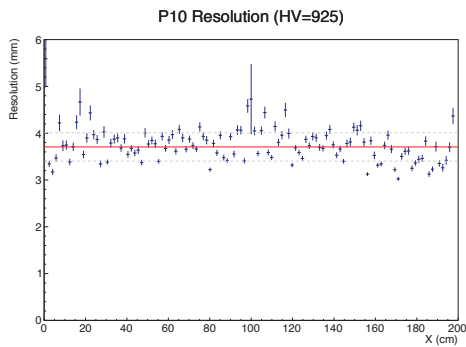
(d)



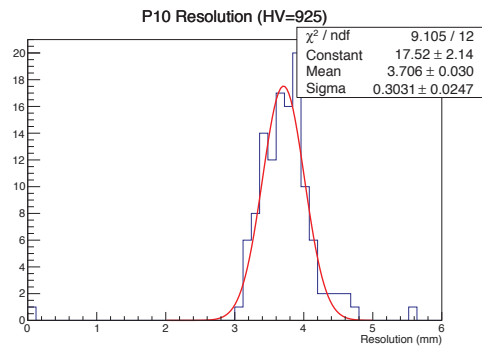
(e)



(f)

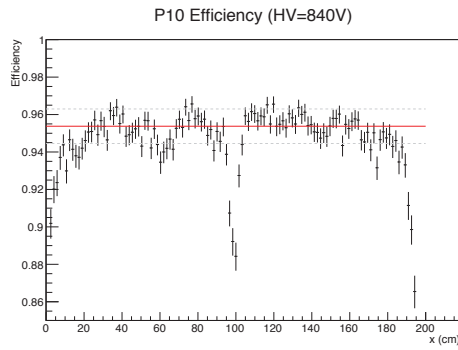


(g)

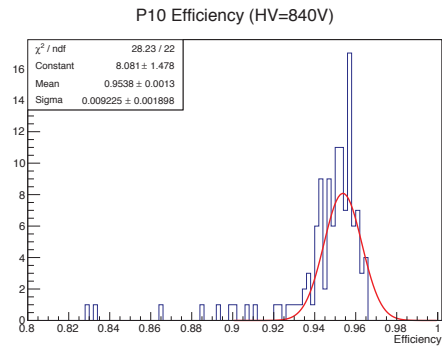


(h)

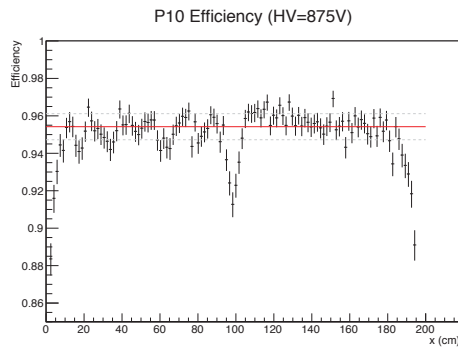
Figure B.13: Resolution measurements for Plane 10



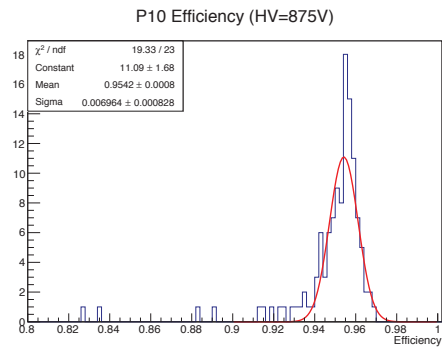
(a)



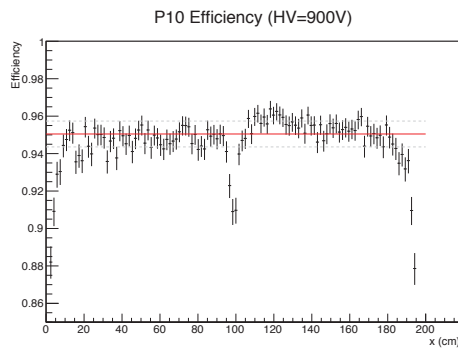
(b)



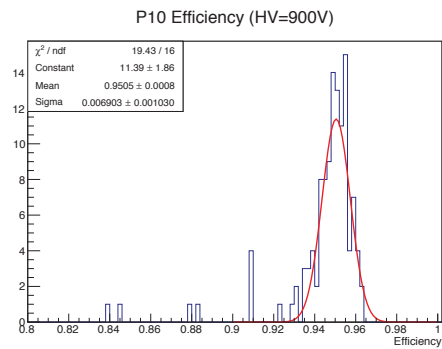
(c)



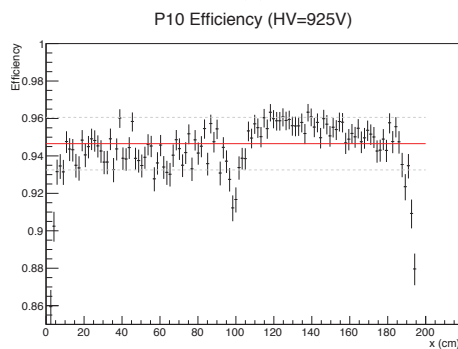
(d)



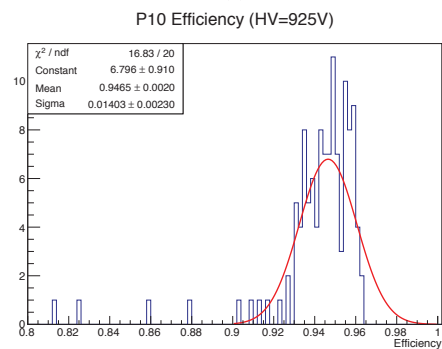
(e)



(f)

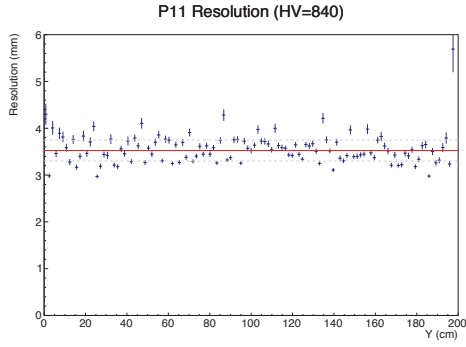


(g)

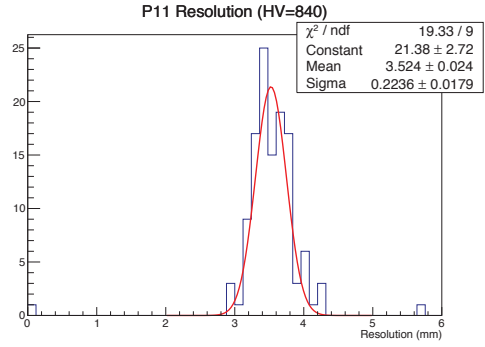


(h)

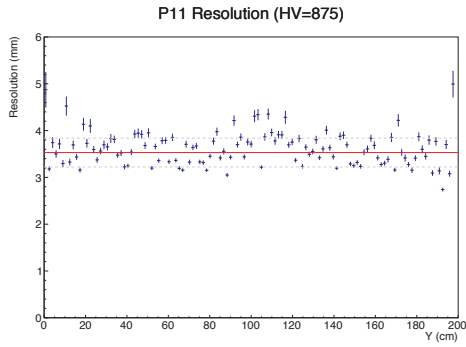
Figure B.14: Efficiency measurements for Plane 10



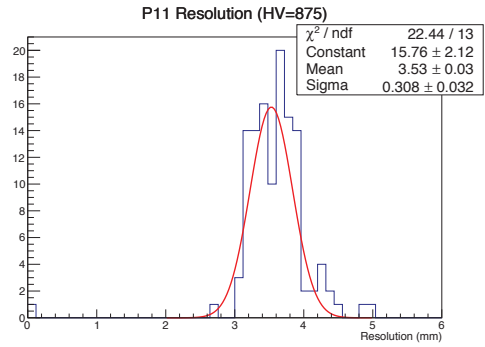
(a)



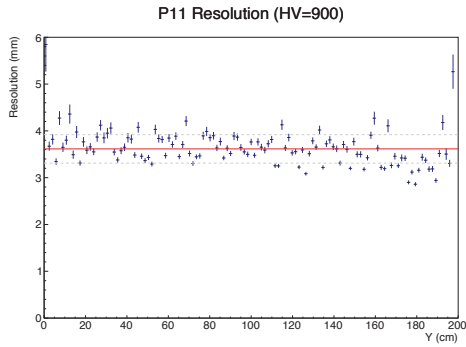
(b)



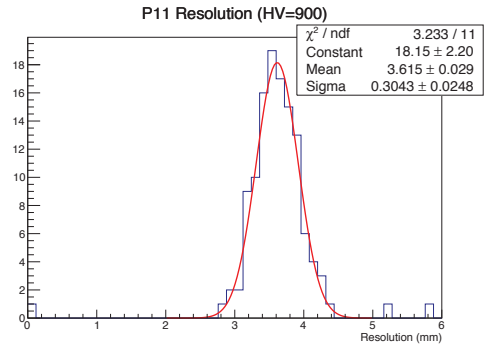
(c)



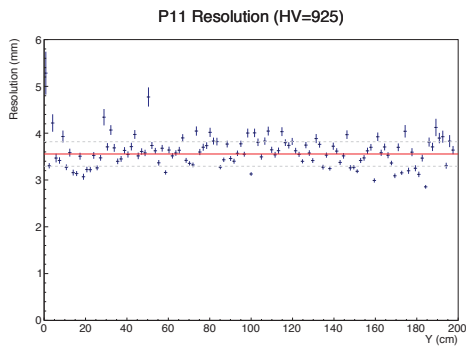
(d)



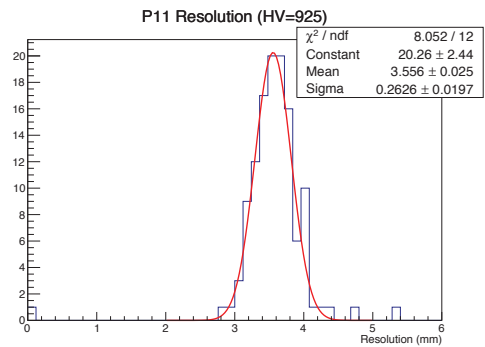
(e)



(f)

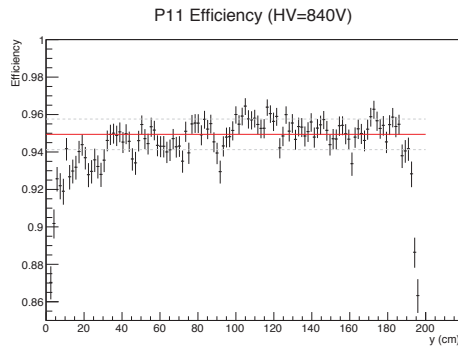


(g)

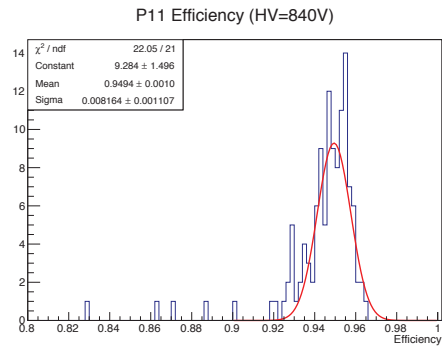


(h)

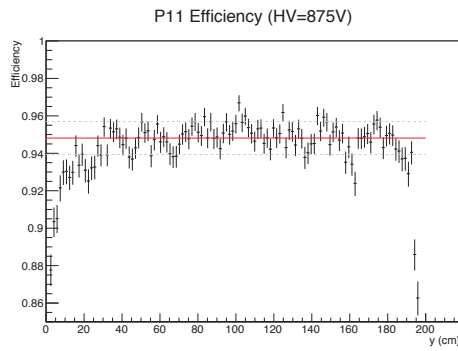
Figure B.15: Resolution measurements for Plane 11



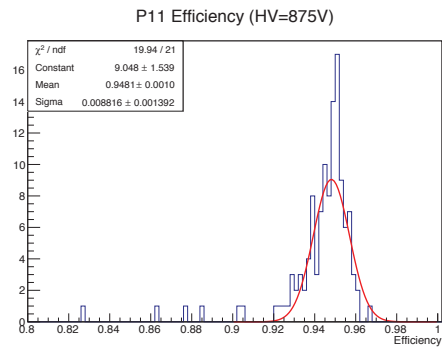
(a)



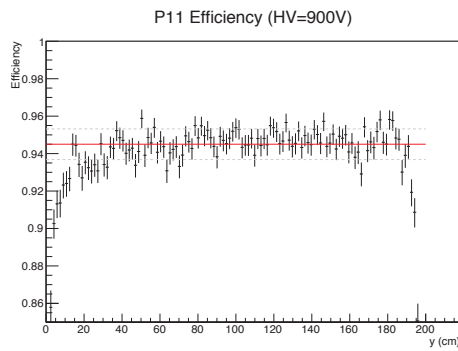
(b)



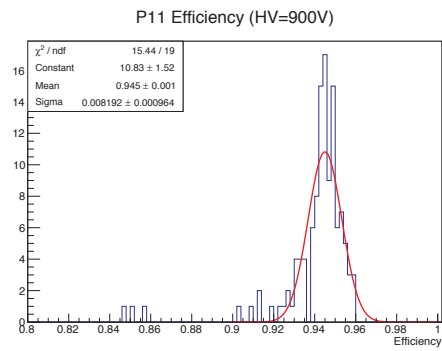
(c)



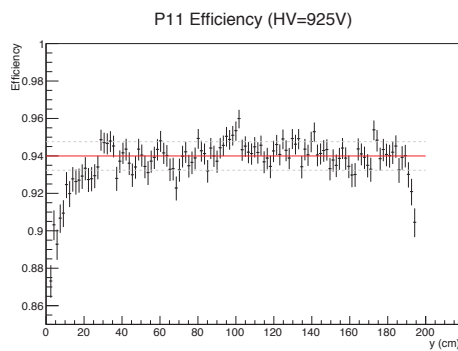
(d)



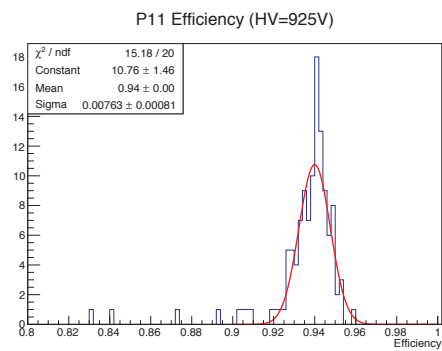
(e)



(f)



(g)

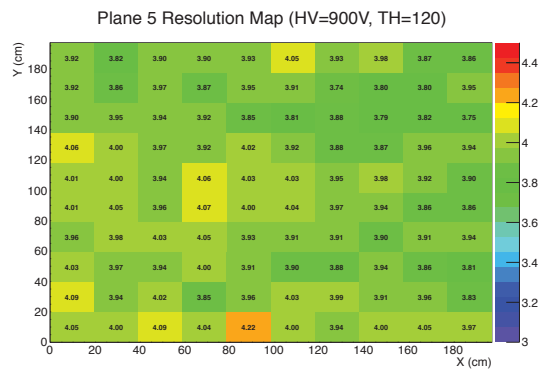
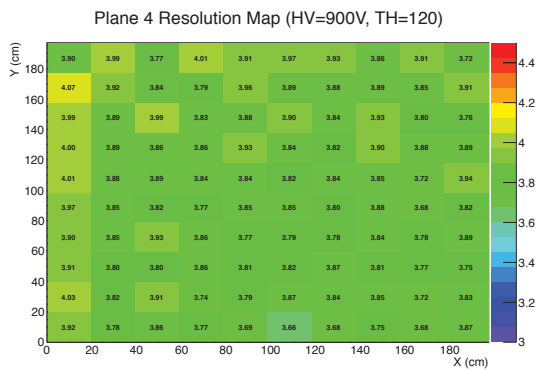


(h)

Figure B.16: Efficiency measurements for Plane 11

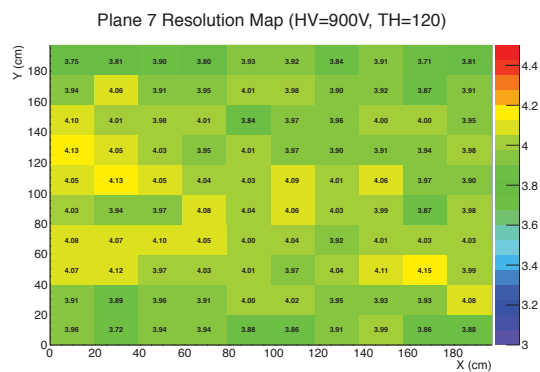
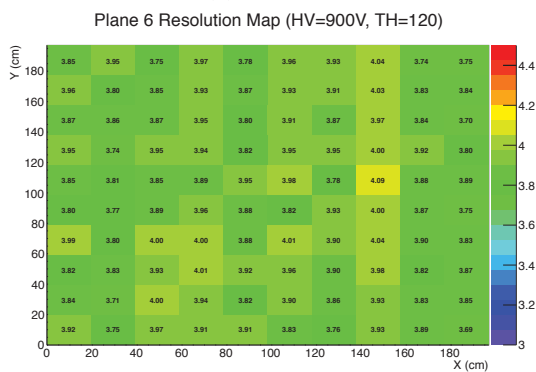
This page intentionally left blank.

Annex C: Resolution map plots



(a) Plane 4

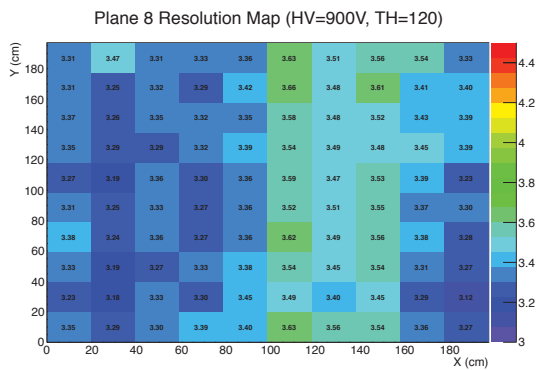
(b) Plane 5



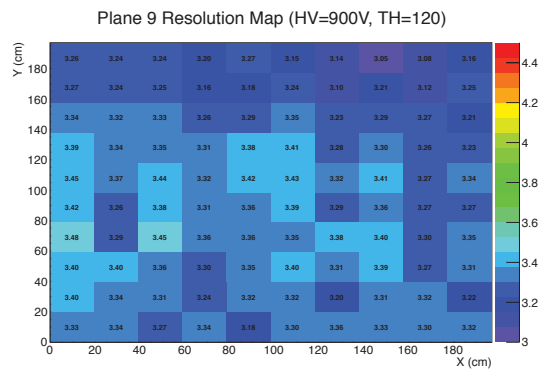
(c) Plane 6

(d) Plane 7

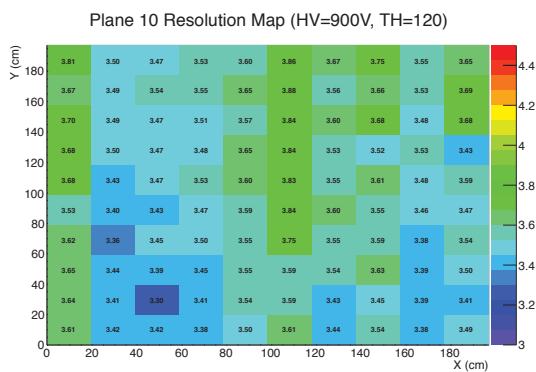
Figure C.1: Lower tracker resolution maps



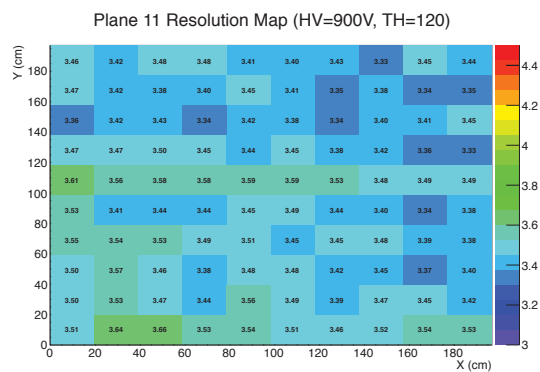
(a) Plane 8



(b) Plane 9



(c) Plane 10

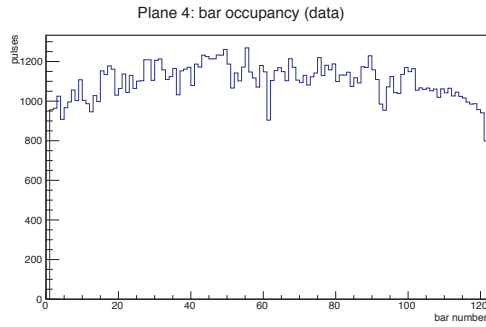


(d) Plane 11

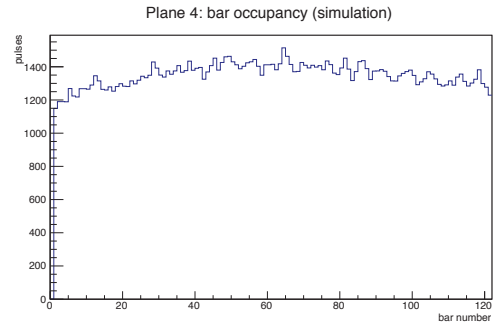
Figure C.2: Upper tracker resolution maps

This page intentionally left blank.

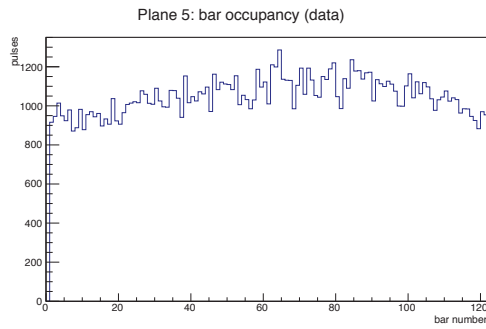
Annex D: Occupancy plots for data and simulation



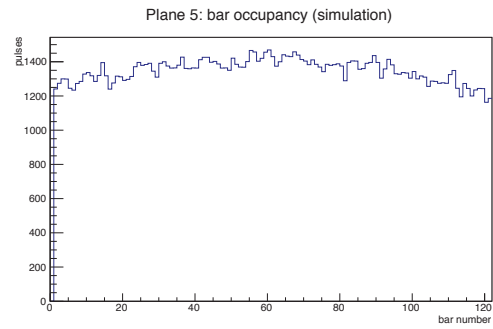
(a) Plane 4, data



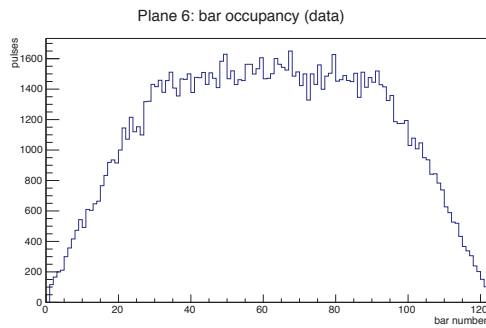
(b) Plane 4, simulation



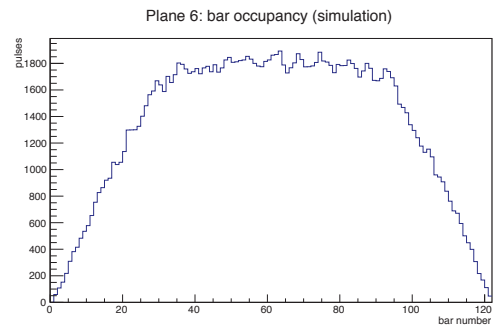
(c) Plane 5, data



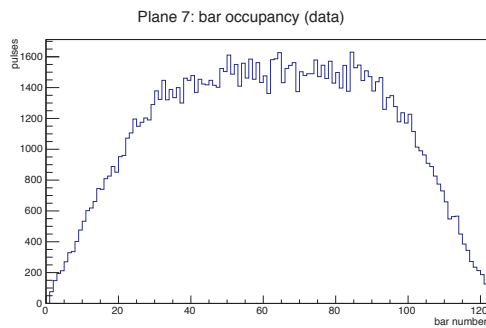
(d) Plane 5, simulation



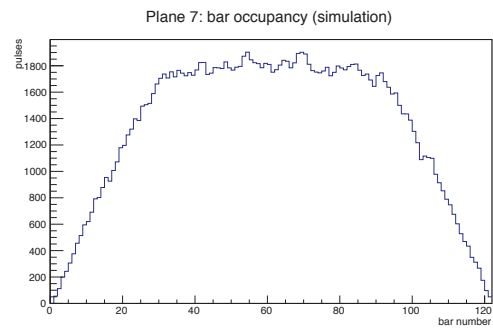
(e) Plane 6, data



(f) Plane 6, simulation

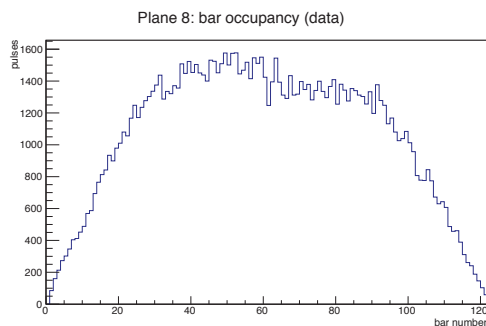


(g) Plane 7, data

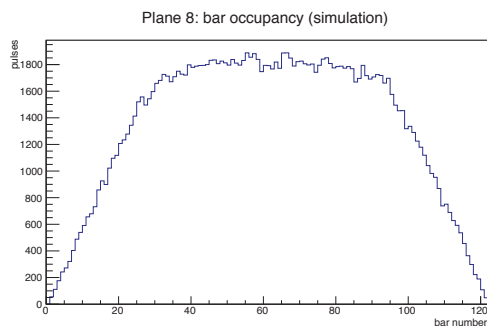


(h) Plane 7, simulation

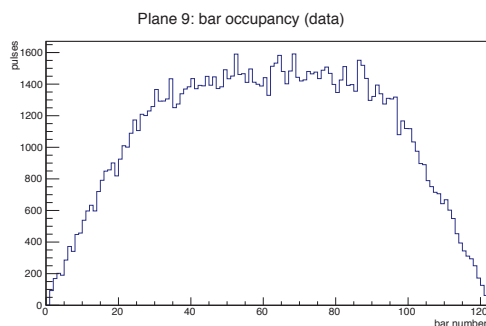
Figure D.1: Occupancy plots for the Lower Tracker (data and simulation).



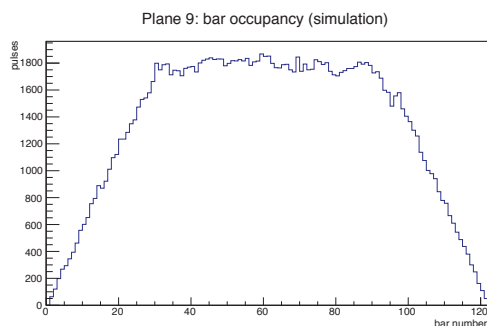
(a) Plane 8, data



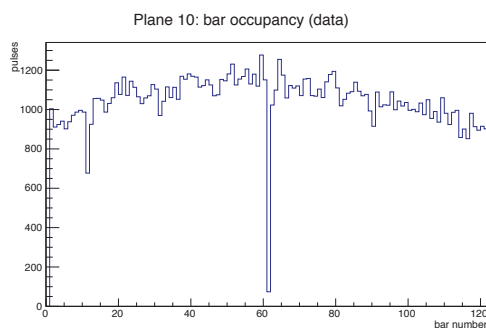
(b) Plane 8, simulation



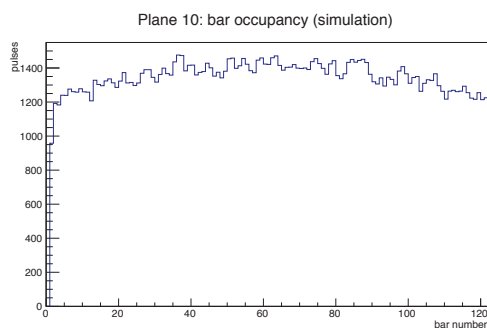
(c) Plane 9, data



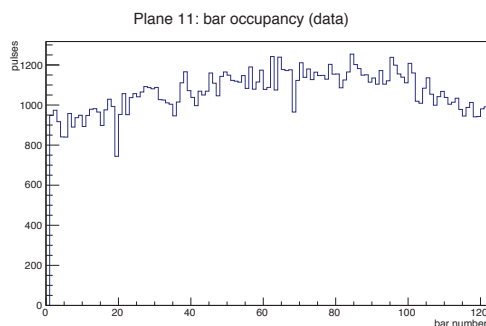
(d) Plane 9, simulation



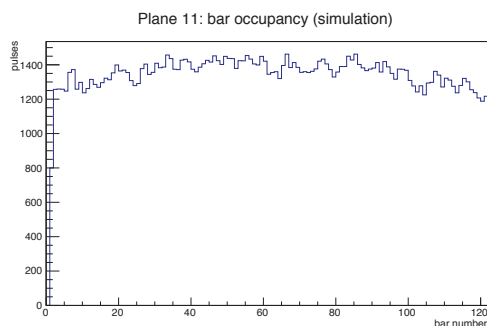
(e) Plane 10, data



(f) Plane 10, simulation



(g) Plane 11, data

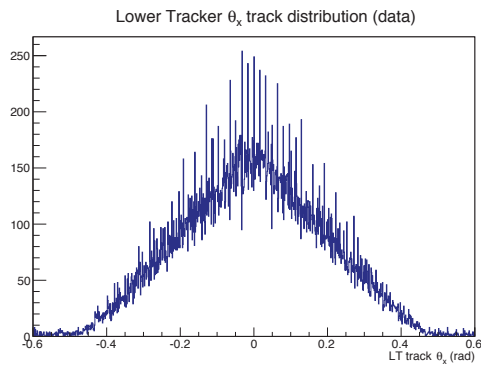


(h) Plane 11, simulation

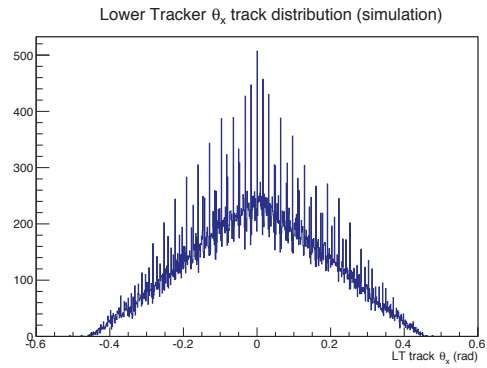
Figure D.2: Occupancy plots for the Lower Tracker (data and simulation).

This page intentionally left blank.

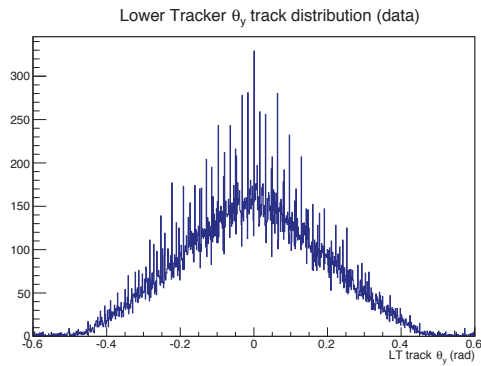
Annex E: Reconstructed track theta plots for data and simulation



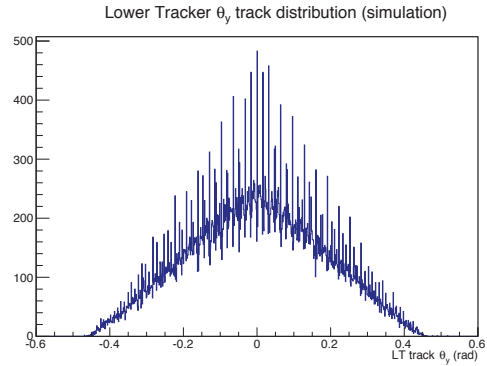
(a) θ_x , data



(b) θ_x , simulation

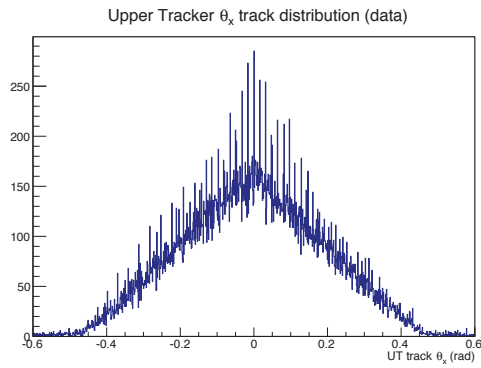


(c) θ_y , data

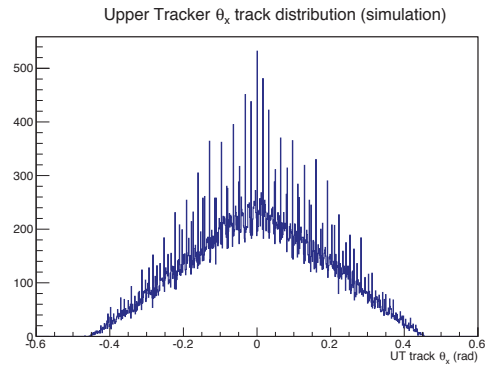


(d) θ_y , simulation

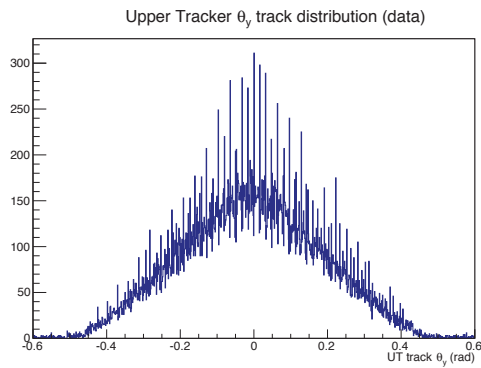
Figure E.1: Lower Tracker reconstructed track $\theta_{(x;y)}$ distributions.



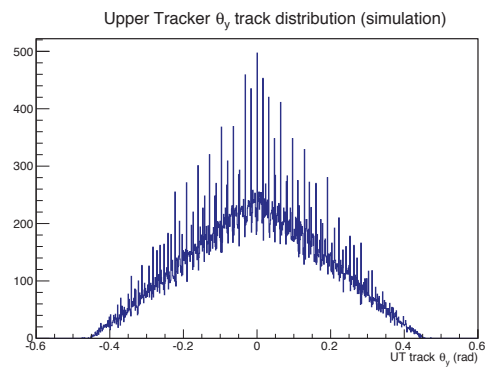
(a) θ_x , data



(b) θ_x , simulation



(c) θ_y , data



(d) θ_y , simulation

Figure E.2: Upper Tracker reconstructed track $\theta_{(x;y)}$ distributions.

This page intentionally left blank.

Distribution list

DRDC Ottawa CR 2013-127

Internal distribution

- 1 David Waller
- 3 DRDC Library

Total internal copies: 4

External distribution

Other Canadian recipients

- 1 Professor John Armitage
Department of Physics
Carleton University
1125 Colonel By Drive
Ottawa, Ontario K1S 5B6
armitage@physics.carleton.ca
- 1 Dr. Guy Jonkmans
Atomic Energy of Canada Limited
1 Plant Road
Chalk River, Ontario K0J 1J0
jonkmansg@aecl.ca
- 1 DSTKIM

Total external copies: 3

Total copies: 7

This page intentionally left blank.

DOCUMENT CONTROL DATA		
(Security classification of title, body of abstract and indexing annotation must be entered when document is classified)		
1. ORIGINATOR (The name and address of the organization preparing the document. Organizations for whom the document was prepared, e.g. Centre sponsoring a contractor's report, or tasking agency, are entered in section 8.) Calian Technologies Ltd. 340 Legget Drive, Suite 101, Ottawa, ON Canada K2K 1Y6		2a. SECURITY CLASSIFICATION (Overall security classification of the document including special warning terms if applicable.) UNCLASSIFIED
		2b. CONTROLLED GOODS (NON-CONTROLLED GOODS) DMC A REVIEW: GCEC APRIL 2011
3. TITLE (The complete document title as indicated on the title page. Its classification should be indicated by the appropriate abbreviation (S, C or U) in parentheses after the title.) Optimization of CRIPT detector performance		
4. AUTHORS (Last name, followed by initials – ranks, titles, etc. not to be used.) Hydomako, R.		
5. DATE OF PUBLICATION (Month and year of publication of document.) January 2014	6a. NO. OF PAGES (Total containing information. Include Annexes, Appendices, etc.) 66	6b. NO. OF REFS (Total cited in document.) 6
7. DESCRIPTIVE NOTES (The category of the document, e.g. technical report, technical note or memorandum. If appropriate, enter the type of report, e.g. interim, progress, summary, annual or final. Give the inclusive dates when a specific reporting period is covered.) Contract Report		
8. SPONSORING ACTIVITY (The name of the department project office or laboratory sponsoring the research and development – include address.) Defence R&D Canada – Ottawa 3701 Carling Avenue, Ottawa ON K1A 0Z4, Canada		
9a. PROJECT OR GRANT NO. (If appropriate, the applicable research and development project or grant number under which the document was written. Please specify whether project or grant.) ARP 06dp	9b. CONTRACT NO. (If appropriate, the applicable number under which the document was written.) EN578-120158/234/EI	
10a. ORIGINATOR'S DOCUMENT NUMBER (The official document number by which the document is identified by the originating activity. This number must be unique to this document.) DRDC Ottawa CR 2013-127	10b. OTHER DOCUMENT NO(s). (Any other numbers which may be assigned this document either by the originator or by the sponsor.)	
11. DOCUMENT AVAILABILITY (Any limitations on further dissemination of the document, other than those imposed by security classification.) <input checked="" type="checkbox"/> (X) Unlimited distribution <input type="checkbox"/> () Defence departments and defence contractors; further distribution only as approved <input type="checkbox"/> () Defence departments and Canadian defence contractors; further distribution only as approved <input type="checkbox"/> () Government departments and agencies; further distribution only as approved <input type="checkbox"/> () Defence departments; further distribution only as approved <input type="checkbox"/> () Other (please specify):		
12. DOCUMENT ANNOUNCEMENT (Any limitation to the bibliographic announcement of this document. This will normally correspond to the Document Availability (11). However, where further distribution (beyond the audience specified in (11)) is possible, a wider announcement audience may be selected.)		

13. ABSTRACT (A brief and factual summary of the document. It may also appear elsewhere in the body of the document itself. It is highly desirable that the abstract of classified documents be unclassified. Each paragraph of the abstract shall begin with an indication of the security classification of the information in the paragraph (unless the document itself is unclassified) represented as (S), (C), or (U). It is not necessary to include here abstracts in both official languages unless the text is bilingual.)

The Cosmic Ray Inspection and Passive Tomography (CRIPT) collaboration has constructed a large-scale detector prototype for investigating the use of cosmic ray muon scattering tomography for Special Nuclear Material (SNM) identification. In order to produce reconstructed images of the highest quality, it is important to ensure that the detector has achieved optimal performance. In this report, the detector operating parameters are investigated, with the goal of optimizing the hit resolution. Furthermore, the results of simple Monte Carlo simulation are presented, which validate the observed geometric acceptance of the detector and give a rough evaluation of the performance of the momentum estimate algorithm.

14. KEYWORDS, DESCRIPTORS or IDENTIFIERS (Technically meaningful terms or short phrases that characterize a document and could be helpful in cataloguing the document. They should be selected so that no security classification is required. Identifiers, such as equipment model designation, trade name, military project code name, geographic location may also be included. If possible keywords should be selected from a published thesaurus. e.g. Thesaurus of Engineering and Scientific Terms (TEST) and that thesaurus identified. If it is not possible to select indexing terms which are Unclassified, the classification of each should be indicated as with the title.)

Cosmic Ray Inspection and Passive Tomography
CRIPT
Cosmic Ray Muons
Detector evaluation and optimization

Defence R&D Canada

Canada's leader in Defence
and National Security
Science and Technology

R & D pour la défense Canada

Chef de file au Canada en matière
de science et de technologie pour
la défense et la sécurité nationale



www.drdc-rddc.gc.ca